Article

Cell Chemical Biology

Imidazole Ketone Erastin Induces Ferroptosis and Slows Tumor Growth in a Mouse Lymphoma Model

Graphical Abstract

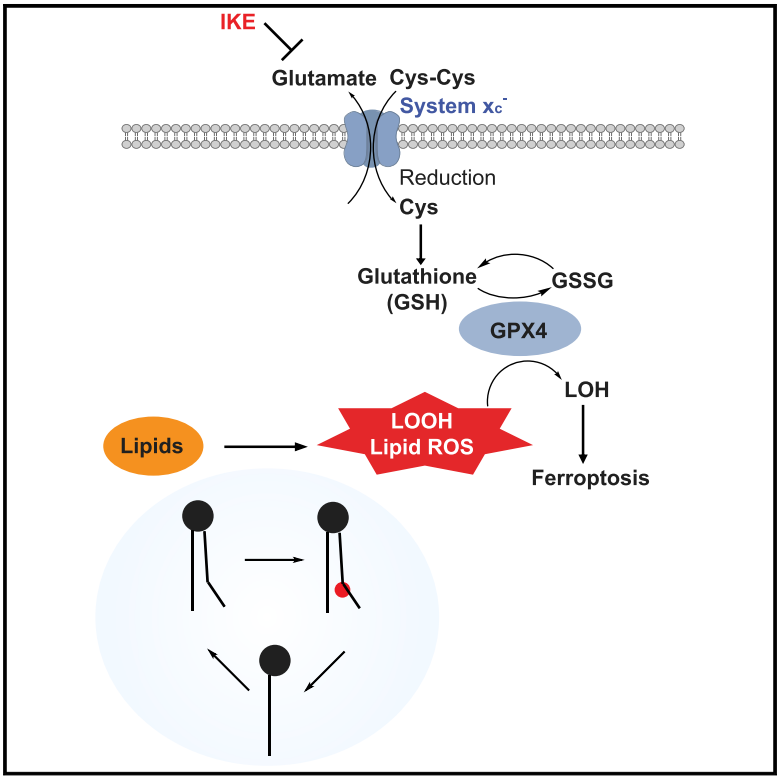

Highlights

- IKE is a potent, selective, and metabolically stable system x_c^- inhibitor
- IKE inhibited tumor growth in a diffuse large B cell lymphoma mouse model
- Untargeted lipidomic profiling revealed lipid metabolism features of ferroptosis
- PEG-PLGA nanoparticles have reduced toxicity in a mouse xenograft model

Authors

Yan Zhang, Hui Tan, Jacob D. Daniels, ..., Koji Uchida, Owen A. O'Connor, Brent R. Stockwell

Correspondence

bstockwell@columbia.edu

In Brief

Zhang et al. identified imidazole ketone erastin (IKE) as a potent and metabolically stable inhibitor of system x_c^- and inducer of ferroptosis. The authors show that IKE exerts an antitumor effect in a mouse xenograft model and exhibits distinct lipid metabolism effects *in vitro* and *in vivo*.

Zhang et al., 2019, Cell Chemical Biology *26*, 1–11
May 16, 2019
https://doi.org/10.1016/j.chembiol.2019.01.008

CellPress

Please cite this article in press as: Zhang et al., Imidazole Ketone Erastin Induces Ferroptosis and Slows Tumor Growth in a Mouse Lymphoma Model, Cell Chemical Biology (2019), https://doi.org/10.1016/j.chembiol.2019.01.008

Cell Chemical Biology
Article

Imidazole Ketone Erastin Induces Ferroptosis and Slows Tumor Growth in a Mouse Lymphoma Model

Yan Zhang,[1] Hui Tan,[1] Jacob D. Daniels,[2] Fereshteh Zandkarimi,[3,4] Hengrui Liu,[1] Lewis M. Brown,[3,4] Koji Uchida,[5] Owen A. O'Connor,[6] and Brent R. Stockwell[1,3,7,*]

[1]Department of Chemistry, Columbia University, New York, NY 10027, USA
[2]Department of Pharmacology, Columbia University Medical Center, New York, NY 10032, USA
[3]Department of Biological Sciences, Columbia University, New York, NY 10027, USA
[4]Quantitative Proteomics and Metabolomics Center, Columbia University, New York, NY 10027, USA
[5]Graduate School of Agricultural and Life Sciences, The University of Tokyo, Tokyo 113-8657, Japan
[6]Center for Lymphoid Malignancies, Columbia University Medical Center, College of Physicians and Surgeons, New York, NY 10019, USA
[7]Lead Contact
*Correspondence: bstockwell@columbia.edu
https://doi.org/10.1016/j.chembiol.2019.01.008

SUMMARY

Ferroptosis is a form of regulated cell death that can be induced by inhibition of the cystine-glutamate antiporter, system x_c^-. Among the existing system x_c^- inhibitors, imidazole ketone erastin (IKE) is a potent, metabolically stable inhibitor of system x_c^- and inducer of ferroptosis potentially suitable for *in vivo* applications. We investigated the pharmacokinetic and pharmacodynamic features of IKE in a diffuse large B cell lymphoma (DLBCL) xenograft model and demonstrated that IKE exerted an antitumor effect by inhibiting system x_c^-, leading to glutathione depletion, lipid peroxidation, and the induction of ferroptosis biomarkers both *in vitro* and *in vivo*. Using untargeted lipidomics and qPCR, we identified distinct features of lipid metabolism in IKE-induced ferroptosis. In addition, biodegradable polyethylene glycol-poly(lactic-co-glycolic acid) nanoparticles were employed to aid in IKE delivery and exhibited reduced toxicity compared with free IKE in a DLBCL xenograft model.

INTRODUCTION

Ferroptosis is a type of regulated cell death driven by iron-dependent lipid peroxidation that can be inhibited by iron chelators and lipophilic antioxidants (Dixon et al., 2012; Stockwell et al., 2017). The ferroptosis-suppressing cystine/glutamate antiporter system x_c^- is required in some contexts to provide cells with cysteine (Stockwell et al., 2017); inhibition of system x_c^- can induce ferroptosis through cysteine deprivation (Dixon et al., 2012), subsequent glutathione (GSH) depletion, and ultimately inactivation of GSH peroxidase 4 (GPX4) (Yang et al., 2014; Dixon et al., 2014). However, existing system x_c^- inhibitors, including sulfasalazine, glutamate, sorafenib, and erastin, are not suitable for *in vivo* evaluation due to the lack of potency, selectivity, and/or metabolic stability. Imidazole ketone erastin (IKE) is an erastin analog with nanomolar potency, high metabolic stability, and intermediate water solubility, thus potentially representing a suitable candidate for *in vivo* evaluation of the impact of ferroptosis driven through system x_c^- inhibition in mouse models of cancer (Larraufie et al., 2015).

Diffuse large B cell lymphoma (DLBCL) is an aggressive malignancy of B lymphocytes, accounting for approximately 30% of all non-Hodgkin's lymphoma cases. DLBCL cell lines are particularly sensitive to system x_c^- inhibition (Skouta et al., 2014; Yang et al., 2014), due to their inability to use the transsulfuration pathway to synthesize cysteine from methionine (Gout et al., 2001). DLBCL is a heterogeneous disease, with 60–70% of patients being cured with combination chemotherapy and the remainder succumbing to the disease (Chapuy et al., 2018). Thus, therapies with distinct mechanisms of action may be beneficial for refractory patients, preventing disease relapse and improving therapeutic outcomes. Here, we identified ferroptosis-sensitive and resistant DLBCL cell lines, and established a subcutaneous DLBCL xenograft model to study the role of ferroptosis in treating DLBCL. We found that IKE exhibits antitumor activity in this DLBCL xenograft model, which correlates with an increase of lipid peroxidation in tumors. These findings suggest that IKE can be effective as a potential therapeutic regimen for DLBCL.

While small-molecule system x_c^- inhibitors are promising agents for inducing ferroptosis in cancers that are highly dependent on cystine import (Narang et al., 2007; Guan et al., 2009; Lu et al., 2018), there are a number of potential concerns in translating such agents to patients. First, many compounds, including some system x_c^- inhibitors, do not accumulate to sufficiently high enough concentrations in target tumor tissues, resulting in a minimal pharmacodynamic effect. Second, while system x_c^- inhibitors are expected to be largely tolerable based on the observation that *Slc7a11* knockout mice have no obvious phenotypes (Sato et al., 2005; McCullagh and Featherstone, 2014), it is possible that systemic inhibition of system x_c^- would cause toxicity in normal tissues, or that off-target effects of system x_c^- inhibitors might cause undesirable toxicities. For these reasons, we hypothesized that improving the formulation and delivery of IKE to tumors might enhance its therapeutic index and potential for translation. For example, nanocarriers could be used to increase tumor targeting through the enhanced permeability and retention (EPR) effect (Yue et al., 2013; Blanco et al., 2015). Indeed, the polyethylene glycol-poly(lactic-co-glycolic acid) nanoparticle (PEG-

PLGA NP) carrier we employed caused increased IKE accumulation in tumors and inhibited tumor growth in mice with less toxicity compared with free IKE. These IKE PEG-PLGA NPs were formulated using a scalable microfluidic NanoAssemblr platform (Gdowski et al., 2018), with a mean size of ~80 nm, polydispersity index of 0.2, surface charge of −17 mV, and loading efficiency of 24% by weight. This formulation could provide a potential therapeutic option and research tool for *in vivo* studies of DLBCL and other ferroptosis-sensitive cancers.

Several studies have shown the important roles of lipids in ferroptosis (Skouta et al., 2014; Yang et al., 2016; Doll et al., 2017; Kagan et al., 2017; Magtanong et al., 2016). The significant depletion of polyunsaturated fatty acids (PUFAs) and PUFA-containing phospholipids has been reported in erastin-treated and erastin-analog-treated HT-1080 cells (Skouta et al., 2014; Yang et al., 2016). Phosphatidylethanolamines (PEs) containing arachidonyl and adrenoyl have been suggested as preferred substrates in RSL3-induced ferroptosis (Kagan et al., 2017; Doll et al., 2017). Moreover, some lipid metabolism genes, including acyl-coenzyme A (CoA) synthetase long-chain family member 4 (*ACSL4*) and lysophosphatidylcholine acyltransferase 3 (*LPCAT3*), have been reported as regulators of ferroptosis (Doll et al., 2017; Kagan et al., 2017). In this study, we applied untargeted mass spectrometry (MS) in conjunction with ultra-performance liquid chromatography (UPLC) to profile lipid changes in DLBCL cells and a DLBCL xenograft mouse model in response to IKE treatment. We observed significant changes in 62 lipid species *in vitro* and 37 lipid species *in vivo* upon IKE treatment, including phospholipids, triacylglycerides (TAGs), diacylglycerides (DAGs), monoacylglycerides (MAGs), and free fatty acids. In addition, a series of genes encoding lipid metabolism enzymes, including the lipid *de novo* biosynthetic enzymes acetyl-CoA carboxylase 1 (ACC1) and elongation of very long chain fatty acids protein 7 (ELOVL7); lipid-remodeling enzymes adipose triglyceride lipase (ATGL), secretory phospholipase A2f (sPLA2F), lysophosphatidylethanolamine acyltransferase 1 (LPEAT1), and LPCAT4; and lipid peroxidation enzymes lipoxygenases 12 and 15 (ALOX12 and ALOX15), were upregulated upon IKE treatment. Co-treatment with ferroptosis inhibitors ferrostatin-1 (fer-1) or β-mercaptoethanol (β-Me) in IKE-treated cells prevented the upregulation of these genes, indicating that upregulation comes from system x_c^- inhibition and downstream lipid peroxidation. Collectively, these results suggest the involvement of lipids and lipid metabolism genes in IKE-induced ferroptosis and the protective effect of ferroptosis inhibitors in preventing IKE-induced lipid changes.

RESULTS

IKE Potently Reduces DLBCL Cell Number

The ferroptosis inducer and system x_c^- inhibitor erastin is a useful small molecule for *in vitro* applications, but it is metabolically labile and has low water solubility and potency, precluding its use *in vivo*. The small molecule IKE is an erastin analog incorporating a carbonyl (Figure 1A) that can potentially form a reversible covalent interaction with proteins, resulting in >100× potency improvement compared with erastin in some cell lines (Larraufie et al., 2015). Substitution of an ethoxy moiety with isopropoxy resulted in improved metabolic stability, and the imidazole moiety in IKE helped increase water solubility and stability of the ketone, making IKE soluble under acidic conditions.

We sought to evaluate DLBCL cell line sensitivity to ferroptosis and to establish a lymphoma xenograft model using a ferroptosis-sensitive DLBCL cell line. A panel of 18 DLBCL cell lines representing distinct DLBCL subtypes, including germinal center B cell-like, activated B cell-like, and unclassified subgroups, was evaluated. The 18 DLBCL cell lines showed differential sensitivity to IKE inhibition, with cell lines exhibiting half-maximal inhibitory concentration (IC_{50}) < 100 nM classified as sensitive cell lines, those with IC_{50} > 10 μM classified as resistant cell lines, and those with IC_{50} values between 100 nM and 10 μM classified as having intermediate resistance (Figure 1B). We further tested the degree of IKE-induced lethality upon co-treatment with the ferroptosis inhibitor fer-1, a radical-trapping antioxidant that inhibits lethal lipid peroxidation during ferroptosis (Skouta et al., 2014; Zilka et al., 2017). Co-treatment with fer-1 rescued cell death induced by IKE in DLBCL cell lines, indicating that IKE-induced lethality in these cell lines resulted from lipid peroxidation and ferroptosis (Figure S1A). Among the sensitive DLBCL cell lines, we selected SUDHL6 for generating a subcutaneous xenograft model in 6-week-old male NCG mice.

IKE Pharmacodynamic Study *In Vitro*

We aimed to investigate whether IKE specifically inhibited system x_c^- and induced ferroptosis in DLBCL cells. Previous studies found that IKE inhibited glutamate release, and the IKE parental analog erastin inhibited cystine uptake. Thus, we tested the cellular level of reduced GSH, which requires cysteine for its biosynthesis, as a readout of IKE potency. A fluorometric method revealed dose-dependent GSH depletion by IKE (Figure 1C); this effect was reversed by co-treatment with 10 μM β-ME, which reduces cystine to cysteine, allowing its import into cells through systems A, ASC, and L, thus circumventing inhibition of system x_c^-. The IC_{50} of GSH depletion by IKE was 34 nM (Figure S1B) in SUDHL6 cells, while sulfasalazine's IC_{50} for GSH depletion is in the millimolar range (Narang et al., 2007; Lo et al., 2010).

We next sought to evaluate whether IKE treatment causes lipid peroxidation, a marker of ferroptosis, in DLBCL cells. Analysis of lipid reactive oxygen species (ROS) by flow cytometry using the lipid peroxidation probe C11-BODIPY revealed a dose-dependent increase in lipid ROS upon IKE treatment in SUDHL6 cells (Figure 1D). Co-treatment with 10 μM fer-1 inhibited this signal, as expected (Figure 1D). We reasoned that lipo-oxidative stress markers, including lipid-peroxide-product-derived protein modifications might also be used as ferroptosis biomarkers. Malondialdehyde (MDA) is a naturally occurring reactive carbonyl compound that is derived from lipid peroxidation of PUFAs. Immunofluorescence staining with an anti-dihydropyridine-MDA-lysine adduct antibody (mAb 1F83) (Yamada et al., 2001) revealed that dihydropyridine-MDA-lysine adduct abundance was increased upon IKE treatment (Figures S1C and S1D).

To facilitate molecular characterization of ferroptosis induction in DLBCL cells, we analyzed gene expression biomarkers of ferroptosis in these cell lines by qRT-PCR. Expression of genes involved in ferroptosis (Stockwell et al., 2017) was analyzed upon IKE treatment. *GPX4*, cystathionine β-synthase (*CBS*), and *ACSL4* were not upregulated with IKE treatment (data not shown). However, the system x_c^- component *SLC7A11*,

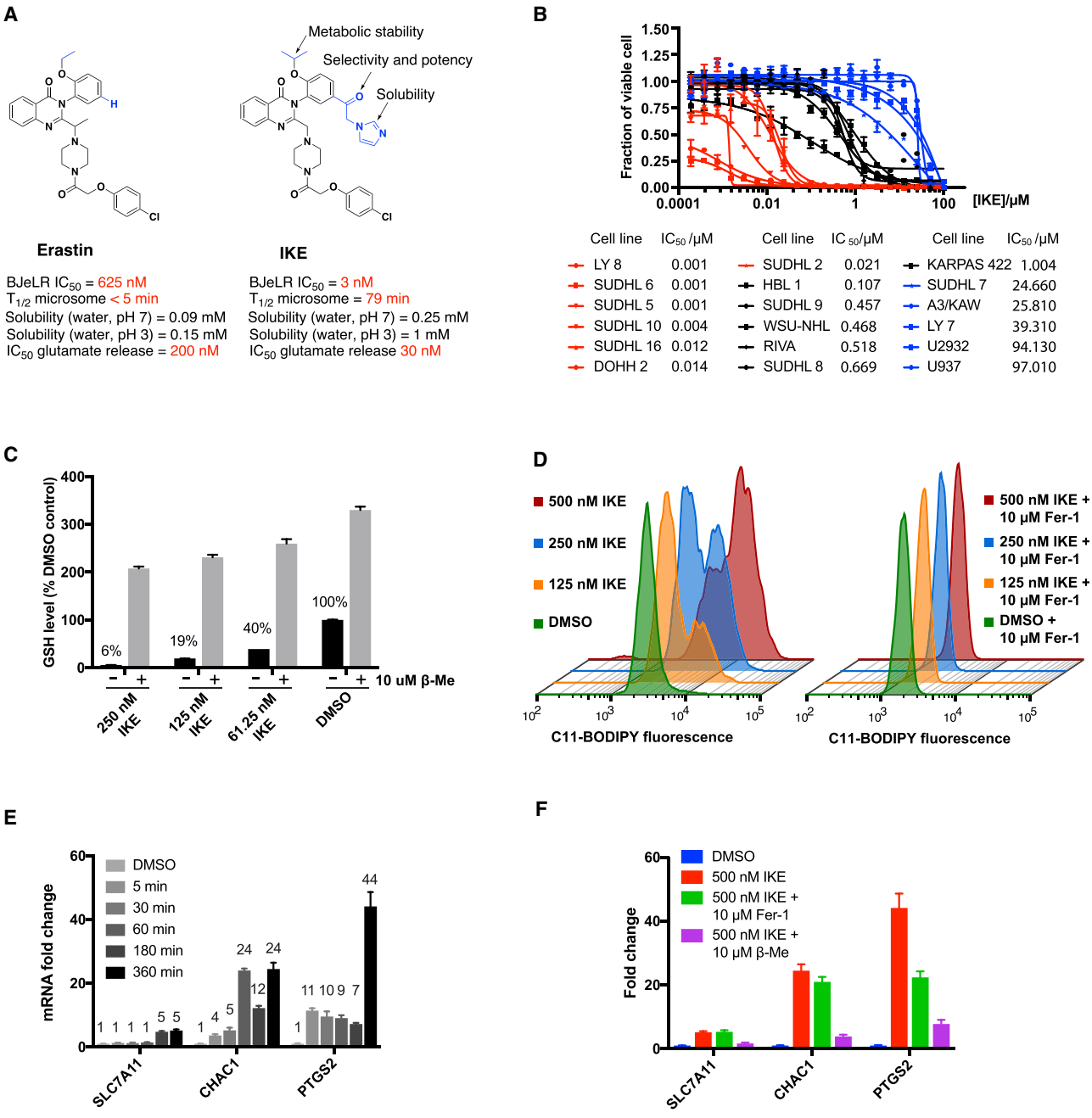

Figure 1. IKE Is a Potent Ferroptosis Inducer

(A) The small molecule IKE with isopropoxy, ketone, and imidazole substitutions is more potent than erastin.

(B) DLBCL cell line sensitivity was measured by incubating cells with a 2-fold series dilution of IKE (starting from 100 μM) for 24 h followed by a CellTiter-Glo luminescent cell viability test. LY8, DOHH2, SUDHL5, SUDHL2, SUDHL6, SUDHL10, and SUDHL16 were classified as sensitive cell lines (red). HBL1, SUDHL9, WSU-NHL, SUDHL8, RIVA, and KARPAS422 were classified as moderately resistant cell lines (black). SUDHL7, U937, A3/KAW, LY7, and U2932 were classified as resistant cell lines (blue).

(C) GSH level was measured with a fluorometric-green probe in SUDHL6 cells treated with different concentrations of IKE with or without 10 μM β-ME for 24 h.

(D) Lipid ROS detected with C11-BODIPY fluorescence were measured in SUDHL6 cells treated with different concentrations of IKE with or without 10 μM fer-1 co-treatment.

(E) qRT-PCR performed in SUDHL6 cells treated with 500 nM IKE for different lengths of time detected *SLC7A11*, *CHAC1*, and *PTGS2* mRNA induction compared with DMSO-treated samples.

(F) Co-treatment of 10 μM fer-1 with 500 nM IKE for 6 h prevented *PTGS2* upregulation, but not *SLC7A11* and *CHAC1* upregulation, while 10 μM β-ME co-treatment prevented the upregulation of all three mRNAs.

Data are plotted as the mean ± SD; n = 2 (B) and (C) or n = 3 (E) and (F) biological replicates. Three independent experiments were performed with similar results for (B) to (F). See also Figure S1.

prostaglandin-endoperoxide synthase 2 (*PTGS2*, which encodes cyclooxygenase-2), and ChaC GSH-specific γ-glutamylcyclotransferase 1 (*CHAC1*) expression was significantly increased in SUDHL6 cells following IKE treatment (Figure 1E). Compared with the upregulation of *PTGS2* and *CHAC1*, induction of *SLC7A11* expression requires a relatively longer-term IKE treatment. *PTGS2* was reported to be upregulated by the lipid peroxidation product 4-hydroxy-2-nonenal (Uchida, 2017) and by GPX4 depletion (Sengupta et al., 2013). Co-treatment with fer-1 inhibited *PTGS2* upregulation, suggesting that *PTGS2* is a functional biomarker of ferroptosis. Fer-1 co-treatment did not inhibit *CHAC1* upregulation, as expected, indicating that *CHAC1* is a parallel downstream marker of system x_c^- inhibition not affected by lipid peroxidation (Figure 1F). In addition, co-treatment with 10 μM β-ME prevented IKE-induced upregulation of *SLC7A11*, *PTGS2*, and *CHAC1*, suggesting that the upregulation of these genes is downstream of cysteine starvation.

Untargeted Lipidomics of IKE-Treated DLBCL Cells

To investigate the effects of IKE on lipid composition and metabolites, we performed untargeted MS-based lipidomics and gene expression analysis of related enzymes during lipid biosynthesis and oxidation. SUDHL6 cells treated with 1 μM IKE, and 500 nM IKE with or without 10 μM fer-1, 10 μM β-Me, or 10 μM deferoxamine (DFO) co-treatment, were subjected to UPLC-MS analysis. The annotations of the lipid species were determined with Lipostar software (v.1.0.4, Molecular Discovery, UK) (Goracci et al., 2017). We observed significant (one-way ANOVA, $p < 0.05$) alterations in the relative abundance of 62 lipid species, including lysophosphatidylcholines (LPCs), phosphatidylcholines (PCs), phosphatidylethanolamines (PEs), and TAGs mainly containing PUFAs, in IKE-treated samples, while co-treatment with β-ME reversed these effects and maintained the levels of these specific lipids to near the amounts on vehicle-treated cells (Figures 2A and 2B). The decrease in the phospholipids PC and PE upon IKE treatment is consistent with the effects of piperazine-erastin treatment and erastin treatment on lipid composition in HT-1080 cells (Yang et al., 2016; Skouta et al., 2014). The decrease in TAG lipids upon IKE treatment indicates TAG lipids may be susceptible to oxidation during ferroptosis. Fer-1 co-treatment significantly increased TAG lipids and decreased MAG lipids, suggesting a possible protective role of TAG as a buffer against oxidative damage (Listenberger et al., 2003). With the induction of oxidants and oxidative stress, lipids can be oxidized via both iron-mediated and enzyme-mediated lipid peroxidation. While co-treatment with DFO inhibited IKE-induced cell death in culture (Figure S1E), it only partially eliminated lipidomic changes upon IKE treatment, possibly due to DFO inhibiting iron-mediated lipid peroxidation, but not enzyme-mediated lipid peroxidation, suggesting that only a subset of lipidomic changes are needed for inducing cell death.

By measuring the mRNA levels of lipid biosynthesis enzymes upon IKE treatment, we discovered that *de novo* lipid biosynthesis pathways, phospholipid remodeling pathways, and arachidonic acid oxidation pathways were activated (Figure 2C). First, there was significant upregulation of *ACC1*, which catalyzes the rate-limiting step of fatty acid biosynthesis from acetyl-CoA to malonyl-CoA, and *ELOVL7*, which catalyzes the rate-limiting reaction of long-chain fatty acid elongation, especially the elongation of C18:3 (*n*-3) and C18:3 (*n*-6)-CoAs (Figures 2C and S2). Second, lipid peroxidation during ferroptosis is a deleterious process, and one way to repair such damage is to remodel lipids, by selectively cleaving the oxidized PUFA tail, replacing it with non-oxidized fatty acids, and subsequently reducing lipid hydroperoxides with GSH peroxidase (Chakraborti, 2003). The activation of the phospholipid remodeling pathway, including sPLA2, which selectively releases PUFAs at the *sn*-2 position of phospholipids; ATGL, which hydrolyzes TAGs; and LPCAT4 and LPEAT1, which catalyze the conversion of LPC to PC, and LPE to PE, respectively, is thus important for the oxidative-damage-repair process. Third, in addition to Fenton chemistry-mediated lipid peroxidation, enzyme-mediated lipid peroxidation was also activated in IKE-induced ferroptosis, as there was increased expression of lipoxygenases *ALOX12* and *ALOX15*. Genes upregulated following IKE treatment are highlighted in red in the schematic lipid metabolism overview (Figure 2D). The upregulation of these genes was partially reversed by co-treatment of 10 μM fer-1 or 10 μM β-ME (Figure 2C), indicating that the observed changes in gene expression result from cysteine depletion and oxidative stress induced by IKE. In summary, these lipidomic changes provide us with a detailed picture of IKE-induced ferroptosis in cell culture at the level of lipid metabolism.

IKE Pharmacokinetics and Pharmacodynamics *In Vivo*

To determine the suitability of IKE for *in vivo* studies, we first evaluated multiple dosage routes by administering a single dose of IKE (50 mg/kg, 5% DMSO in Hank's balanced salt solution [HBSS] at pH 4) using intraperitoneal (i.p.), intravenous, and oral routes in non-obese diabetic/ severe combined immunodeficiency (NOD/SCID) mice. Determination of IKE concentration over a period of 8 h revealed i.p. to be the most effective and practical means of IKE administration (Table S1). Next, IKE concentration in plasma and tumor samples was determined after a single dose of IKE (50 mg/kg, 5% DMSO in HBSS at pH 4, i.p.) in SUDHL6-xenograft-bearing NCG mice over a period of 24 h. IKE reached the highest plasma concentration of 5.2 μg/mL at 1.35 h, and the highest tumor accumulation of 2.5 μg/mL at 3.30 h (Figure 3A, Table S2).

We collected tumor samples from each time point after a single dose of IKE (50 mg/kg, 5% DMSO in HBSS) and evaluated the abundance of ferroptosis markers. There was significant GSH depletion upon IKE dosing starting from 4 h (Figure 3B). The GSH depletion in tumors induced by IKE was persistent at 24 h, even when there was little IKE left in the bulk tumor sample. Consistent with IKE accumulation in the tumor samples, *CHAC1*, *SLC7A11*, and *PTGS2* mRNAs were upregulated starting at 3 h (3- to 5-fold for *PTGS2* and *SLC7A11*, and 2-fold for *CHAC1*) (Figure 3C). Immunofluorescence analysis of samples at 4 h post-treatment showed that there was increased abundance of a hydropyridine-MDA-lysine adduct and 8-hydroxy-2′-deoxyguanosine (8-OHdG), biomarkers for oxidative lesions, indicating that IKE induced lipid peroxidation and more general oxidative stress in these tumor samples (Figures 3D–3E).

IKE Untargeted Lipidomic Study *In Vivo*

We sought to investigate lipidomic changes caused by IKE treatment *in vivo*. We performed untargeted lipidomics on tumor

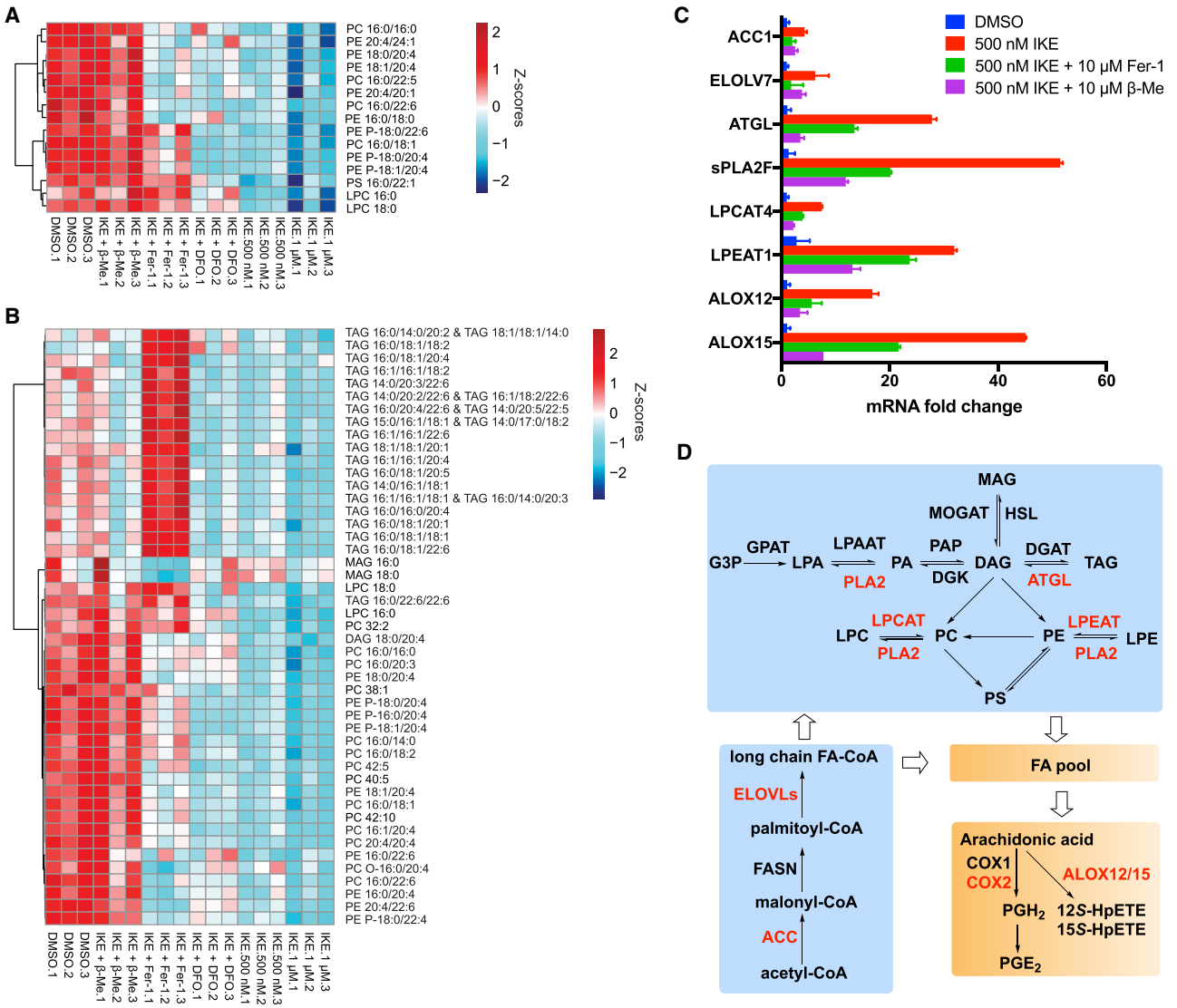

Figure 2. Heatmap of Significantly Changed (One-Way ANOVA, $p < 0.05$) Lipid Species in SUDHL6 Cells Treated with DMSO, 500 nM IKE, 1 μM IKE, 500 nM IKE with 10 μM fer-1 Co-treatment, 500 nM IKE with 10 μM β-ME Co-treatment, or 500 nM IKE with 10 μM DFO Co-treatment, Measured by Liquid Chromatography (LC)-MS

(A and B) Each row represents *Z*-score-normalized intensities of the detected lipid species in (A) negative electrospray ionization mode and (B) positive electrospray ionization mode. Each column represents an independent biological replicate. The lipid abundance is color coded, with red indicating high signal intensity and dark blue indicating low signal intensity. Abbreviations: PC, phosphatidylcholine; PE, phosphatidylethanolamine; PS, phosphatidylserine, LPC, lysoPC; PE P-, plasmalogen PE; TAG, triacylglyceride; DAG, diacylglyceride, MAG, monoacylglyceride.

(C) Fold change in expression of *ACC1*, *ELOVL7*, *ATGL*, *sPLA2F*, *LPCAT4*, *LPEAT1*, *ALOX12*, and *ALOX15* with 500 nM IKE treatment, 500 nM IKE with 10 μM fer-1 co-treatment, and 500 nM IKE with 10 μM β-ME co-treatment compared with DMSO control in SUDHL6 cells. Data are plotted as the mean ± SD, n = 3 biologically independent samples.

(D) Schematic view of fatty acid biosynthesis, lipid remodeling, and arachidonic acid oxidation. The genes upregulated upon IKE treatment are labeled in red. See also Figure S2.

tissue with a single dose of IKE at different time points. We identified significant (one-way ANOVA, $p < 0.05$) increases in the relative abundance of free fatty acids, phospholipids, and diacylglycerides (DAGs) upon IKE treatment (Figures 3F and 3G). Differences with the cell culture experiment might stem from the different tumor microenvironment *in vivo*. The lipids identified were enriched in linoleic acid and arachidonic acid metabolism (Figure S3A). The significant increase in the levels of DAGs and free fatty acids may result from ATGL-mediated TAG hydrolysis (Figure S3B). The increased fatty acids might in turn promote phospholipid remodeling to synthesize specific phospholipids, including PCs and PEs. To explore the free fatty acids effects on cells and ferroptosis, we performed a cell survival test of free fatty acids in the presence or absence of IKE. We found that PUFAs, including γ-linolenic acid, eicosapentaenoic acid, and arachidonic acid, were toxic to cells at high concentration

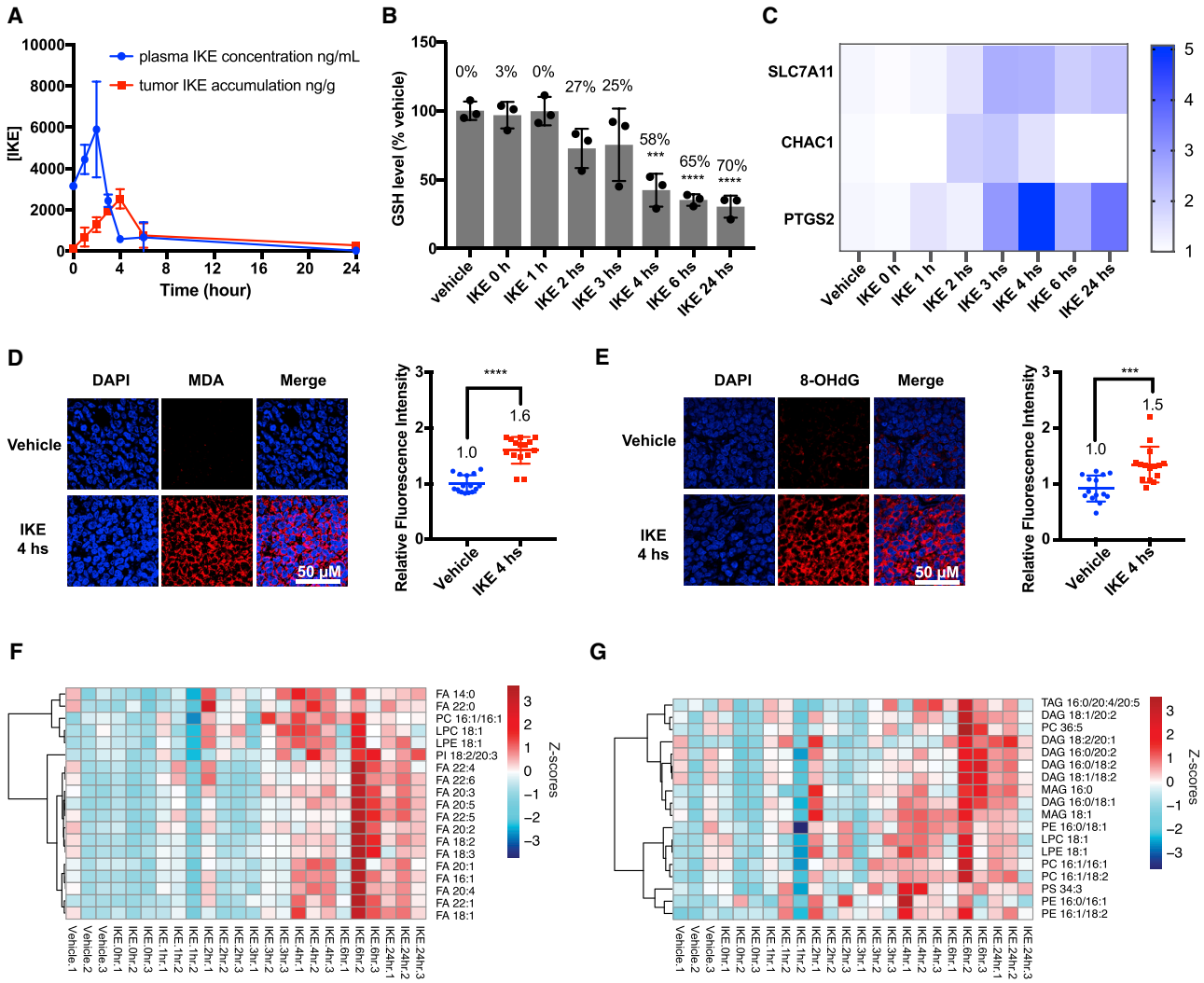

Figure 3. IKE-Induced Ferroptosis Biomarker Changes in a Lymphoma Xenograft Model

(A) A pharmacokinetic study performed in SUDHL6 subcutaneously xenografted NCG mice measured IKE accumulation over time in plasma and tumor using LC-MS.

(B) Analysis of GSH extracted from tumor tissue by fluorometric green showed over 50% GSH depletion with IKE treatment starting at 4 h ***$p < 0.001$, ****$p < 0.0001$ by one-way ANOVA. Data are plotted as the mean ± SD, n = 3 individual mice (A) and (B).

(C) qRT-PCR performed using RNA extracted from tumor tissue showed that *PTGS2*, *SLC7A11*, and *CHAC1* mRNA increased starting from 3 h, colored as blue in the heatmap. Data are plotted as the mean, n = 3 individual mice.

(D–G) (D and E) Immunofluorescence of dihydropyridine-MDA-lysine adduct in paraffin-embedded tumor samples from mice 4 h after treatment with one dose of vehicle or IKE. Quantification of fluorescence intensity showed 1.6-fold increase of dihydropyridine-MDA-lysine adducts and 1.5-fold increase of 8-OHdG in IKE-treated mouse tumor tissue relative to the vehicle-treated mouse tumor tissue (sections were cut from three mice in each group, five images from each section were captured on Zeiss LSM 800 63×/1.40 oil DIC objective). ***$p < 0.001$, ****$p < 0.0001$ by t test. Heatmaps of dysregulated lipids in SUDHL6 subcutaneously xenografted NCG mice treated with one dosage of IKE for at 0, 1, 2, 3, 4, 6, and 24 h or with vehicle, detected by untargeted UPLC-MS analysis. Data shown in heatmaps are lipid species that were identified as being statistically significant ($p < 0.05$) among the groups in (F) negative electrospray ionization mode and (G) positive electrospray ionization mode. Each column represents an independent biological replicate. Each row represents the *Z* score normalized intensity of a lipid feature. The relative abundance of each identified lipid is color coded in blue, indicating low signal intensity, or red, indicating high signal intensity.

Abbreviations: PC, phosphatidylcholine; PE, phosphatidylethanolamine; PI, phosphatidylinositol; PS, phosphatidylserine, LPC, lysoPC; LPE, lysoPE; FA, free fatty acid; TAG, triacylglyceride; DAG, diacylglyceride, MAG, monoacylglyceride. See also Figure S3 and Table S2.

(100 μM) (Figure S3C). Most free fatty acids (10 μM) sensitized cells to ferroptosis, while oleic acid and palmitoleic acid (10 μM) protected against ferroptosis, which might be due to the fact that these two fatty acids lack bis-allylic sites, which are the sites for lipid peroxidation initiation (Gaschler and Stockwell, 2017) (Figure S3D).

IKE PEG-PLGA NPs Have Suitable Properties for Application *In Vivo*

IKE is soluble under acidic aqueous conditions, but not to the same degree under neutral aqueous conditions (Figure 1A). To improve delivery of the compound, we sought to use an NP formulation. We selected biocompatible and biodegradable

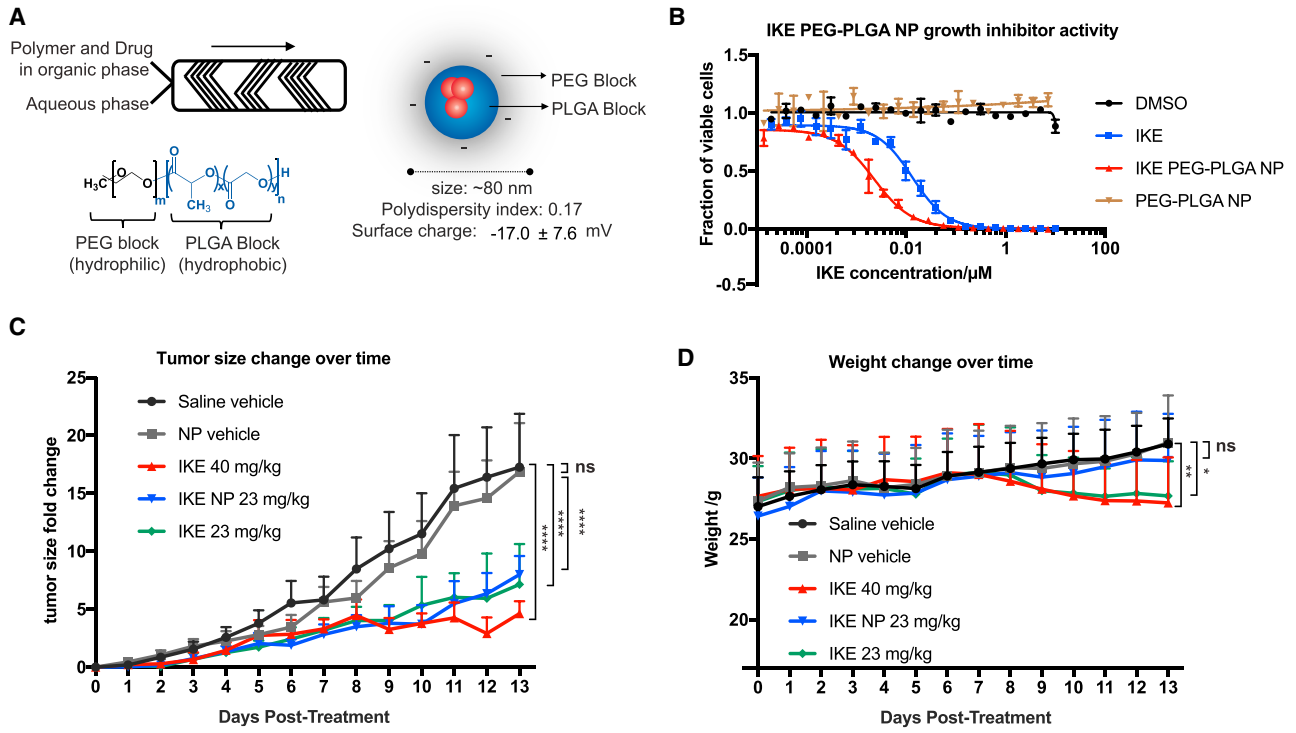

Figure 4. IKE PEG-PLGA NPs <100 nm in Diameter Were Formulated and Showed Reduced Toxicity in SUDHL6 Subcutaneous-Xenografted Mice

(A) A NanoAssemblr equipped with a microfluidic mixer was used to formulate PEG-PLGA NPs (polymer structure shown). The nanoparticles were characterized with a Zetasizer Nano ZS as having a mean diameter of 80 nm, polydispersity index of 0.17, and surface charge of −17 mV.

(B) IKE PEG-PLGA NP cellular activity was measured by CellTiter-Glo luminescent cell viability assay in SUDHL6 cells with 24-h incubation. The encapsulated IKE in PEG-PLGA NPs was measured by LC-MS. The x axis shows IKE concentration. Data are plotted as the mean ± SD, n = 2 technical replicates. Three biologically independent experiments were performed with similar results.

(C) Tumor volume fold change compared with day 0, measured by electronic caliper daily and calculated using the formula volume = 0.5 × length × width^2, revealed a reduction of tumor growth by IKE 40 mg/kg (n = 9), IKE 23 mg/kg (n = 11), and IKE NP 23 mg/kg (n = 13) treatment for 14 days compared with vehicle (n = 13) and NP vehicle (n = 13) controls (data analyzed by two-way ANOVA). ns, $p > 0.5$, *$p < 0.05$, **$p < 0.01$, ***$p < 0.001$, ****$p < 0.0001$.

(D) Mouse weight was measured daily and indicated no weight loss upon NP and IKE NP treatments, but weight loss upon IKE 40 mg/kg and IKE 23 mg/kg treatment starting from day 9. Data are plotted as the mean ± SD. ns, not significant.

See also Figure S4.

PEG-PLGA *di*-block copolymer-based NPs as an IKE carrier system (Figure 4A). The PEG block was used to create a deformable hydrating layer by tight associations with water molecules, which prevents clearance by the mononuclear phagocyte system, prolonging circulation lifetime. The PLGA block was used to form a hydrophobic core to incorporate IKE, which provides sustained release by diffusion and surface and bulk erosion.

To formulate <100-nm NPs with a reproducible method, we employed the high-flow microfluidic system NanoAssemblr (Gdowski et al., 2018; Valencia et al., 2013). Self-assembly of NPs by nanoprecipitation occurs when the organic phase containing IKE and the PEG-PLGA polymer combines with the aqueous phase in a microchannel. IKE PEG-PLGA NPs with a diameter as small as 80 nm and polydispersity index of 0.17 were formulated using this approach (Figure S4). The surface possessed a slightly negative charge with ζ potential of −17.0 mV to prevent NP aggregation. One of the problems with the use of NPs as drug carriers *in vivo* is the low content of drug and low concentration of NPs in suspension. We were able to achieve concentration factors up to 20 using centrifugal filter units without causing NP aggregation or dramatically decreasing IKE loading efficiency (Figure S4C). As a result, IKE PEG-PLGA NPs containing IKE as high as 3 mg/mL (drug loading 3.65% by weight and encapsulation efficiency of 24%) were formulated. Compared with free IKE, IKE PEG-PLGA NPs had enhanced cellular activity in SUDHL6 cells (Figure 4B), which might result from increased internalization of IKE NPs into the cells. Co-treatment with fer-1 rescued cell death induced by IKE and IKE PEG-PLGA NPs (Figure S4G). In addition, administration of 750 mg/kg naked PEG-PLGA NPs daily for 2 weeks did not result in any detectable weight loss or other observable signs of toxicity, suggesting that this NP system was suitable for *in vivo* drug delivery.

IKE Inhibits Tumor Growth *In Vivo* and the PEG-PLGA NP Formulation Enhances Its Therapeutic Index

We investigated the efficacy of IKE *in vivo* in male NCG mice bearing SUDHL6 subcutaneous xenografts. Once tumor volumes reached 100 mm^3, mice were randomized into five groups and treated with vehicle (5% DMSO in HBSS at pH 4),

unfunctionalized PEG-PLGA NPs in water, 40 mg/kg free IKE (5% DMSO in HBSS at pH 4), 23 mg/kg free IKE (5% DMSO in HBSS at pH 4), or 23 mg/kg IKE NPs (IKE PEG-PLGA NPs in water) via i.p. injection once daily. During the experimental period, mouse weight and tumor volume were measured daily to determine IKE's antitumor effect and possible toxicity. Tumor growth was calculated as the fold change relative to original tumor volume on day 0 before the first dose (Figure 4C). Administration of 40 mg/kg IKE, 23 mg/kg IKE, and 23 mg/kg IKE NPs caused a significant decrease in tumor growth starting from day 9 of treatment. The tumor growth inhibition effect was not significantly different between 23 mg/kg free IKE and 23 mg/kg IKE NPs; however, IKE NPs showed less toxicity, as evidenced by weight loss (Figure 4D). Compared with saline vehicle, free IKE (5% DMSO in HBSS at pH 4)-treated mice started losing weight from day 9, which might be caused by the precipitation of IKE after administration into the peritoneum, an environment with pH ranges of 7.5–8.0, causing damage to abdominal organs, or possible toxicity of systemic system x_c^- inhibition, or off-target toxicity of IKE. However, IKE NP-treated mice had a similar weight compared with the saline vehicle and the NP vehicle groups; the lower toxicity of the IKE NP formulation might result from the NPs' capability to prevent the aggregation of hydrophobic drugs (Sun et al., 2014), or the NP EPR effect, which decreases the non-specific distribution and systemic toxicity associated with conventional hydrophobic drugs (Yue et al., 2013). By analyzing IKE tumor accumulation using liquid chromatography-MS, we found that IKE NPs at 23 mg/kg had slightly enhanced tumor accumulation compared with free IKE at 23 mg/kg and were comparable to the free IKE 40 mg/kg treatment (Figure S5A). Overall, the PEG-PLGA NP formulation increased IKE's therapeutic window.

Given the fact that *PTGS2* mRNA was upregulated upon IKE treatment *in vivo* (Figure 3C), we hypothesized that after IKE treatment, there might be an increased level of the *PTGS2* gene product (COX-2) in the tumor. Using immunofluorescence (Figure 5A), we found that COX-2 protein expression was indeed increased in IKE-treated tumor tissue (Figure 5D). There was no significant COX-2 protein expression increase in IKE NP-treated tumors, which might be due to the slower release of IKE from PEG-PLGA NPs (Figure S4F), making the free IKE concentration lower than free IKE-treated tumors. This implies that COX-2 protein abundance is not a highly sensitive pharmacodynamic marker for low concentrations of IKE, but may more effectively report on exposure to high concentrations of IKE.

We further characterized lipid peroxidation in tumor tissues during this efficacy study. Immunofluorescence analysis of tumor tissue from the five groups showed significantly increased dihydropyridine-MDA-lysine adduct levels in IKE-treated and IKE PEG-PLGA NP-treated groups, compared with the saline vehicle and NP vehicle groups (Figures 5B and 5E). Compared with saline vehicle, the NP vehicle group had increased levels of dihydropyridine-MDA-lysine adducts, which might be due to low-level ferroptosis induction of ultrasmall (<10 nm in diameter) NPs in the sample, as observed in PEG-coated silica NPs previously (Kim et al., 2016). In addition, the thiobarbituric acid-reactive substances (TBARS) assay, which measures the fluorescence of MDA-TBA adducts formed, showed increased MDA levels in tumors in the free IKE and IKE PEG-PLGA NP groups compared with vehicle groups (Figure 5G). The TBARS assay is not as sensitive as immunofluorescence for detecting small increases in MDA adducts, suggesting a possible explanation for our inability to detect this increase in the NP vehicle group. Immunofluorescence analysis of 8-OHdG showed increased oxidative DNA damage in IKE-treated and IKE PEG-PLGA NP-treated groups, confirming that IKE treatment induced oxidative damage (Figures 5C and 5F). In addition, there was no increase in caspase-3 activity in tumor tissues upon IKE treatment, suggesting that the inhibition of tumor growth was not due to apoptosis, as expected (Figure S5B).

DISCUSSION

Recent discoveries have suggested that ferroptosis inducers can have antitumor efficacy (Yu et al., 2017; Gout et al., 2001; Liu et al., 2017) and may synergize with chemotherapy in some cell contexts (Sato et al., 2018; Chen et al., 2015; Yamaguchi et al., 2013; Yu et al., 2015). However, there is a lack of potent, selective, and metabolically stable tools to study ferroptosis *in vivo*. Study of the ferroptosis inducer IKE in an SUDHL6 xenograft model demonstrated that IKE and IKE NPs reduce tumor growth by inducing ferroptosis. The IKE PEG-PLGA NP formulation exhibited a larger therapeutic window compared with the free IKE formulation tested. Given the fact that we used a 5% DMSO in HBSS at pH 4 formulation and that IKE is less soluble at pH 7 versus pH 4, we suspect that the toxicity of high-dose free IKE in this study might stem from the precipitation of IKE after injection into the peritoneal cavity.

The induction of ferroptosis theoretically has the potential to shrink tumors. IKE's half-life ($T_{1/2}$) in plasma and $T_{1/2}$ in tumor in SUDHL6 NCG xenograft mice through i.p. injection were 1.83 and 3.50 h, respectively. Compared with the pharmacokinetics of IKE, the once-per-day dosage frequency might be too low to see a tumor shrinking effect; in other words, we might need either a longer half-life compound or formulation or more frequent dosing to balance rapid tumor growth with induction of cell death, to cause tumor regression. The IKE NP formulation had increased accumulation in tumor tissue relative to plasma (Figure S5A), but it might not be high enough to counter rapid tumor growth *in vivo*; delivery of a higher dose to the tumor might be needed. Based on the above considerations, combining IKE with other therapies or designing ferroptosis inducers with enhanced bioavailability and metabolic stability and higher tumor penetration and accumulation is worth investigating to further optimize the therapeutic impact of ferroptosis inducers in diverse cancer models.

Our untargeted lipidomic study identified lipid metabolism features during ferroptosis. First, we observed decreased PEs, PCs, and TAGs upon IKE treatment, possibly resulting from the cleavage of oxidized PUFA tails in PEs, PCs, and TAGs to prevent the oxidative damage to cells induced by IKE treatment. Co-treatment with β-ME, which allows transport of cysteine through systems A, ASC, and L, completely reversed the lipidomic changes caused by IKE treatment. Fer-1 partially prevented the phospholipid decreases in cells, but dramatically increased TAGs. The increased TAG pool might serve as a buffer against lipid peroxidation induced by IKE (Listenberger et al., 2003). However, the iron chelator DFO did not reverse IKE-induced phospholipid

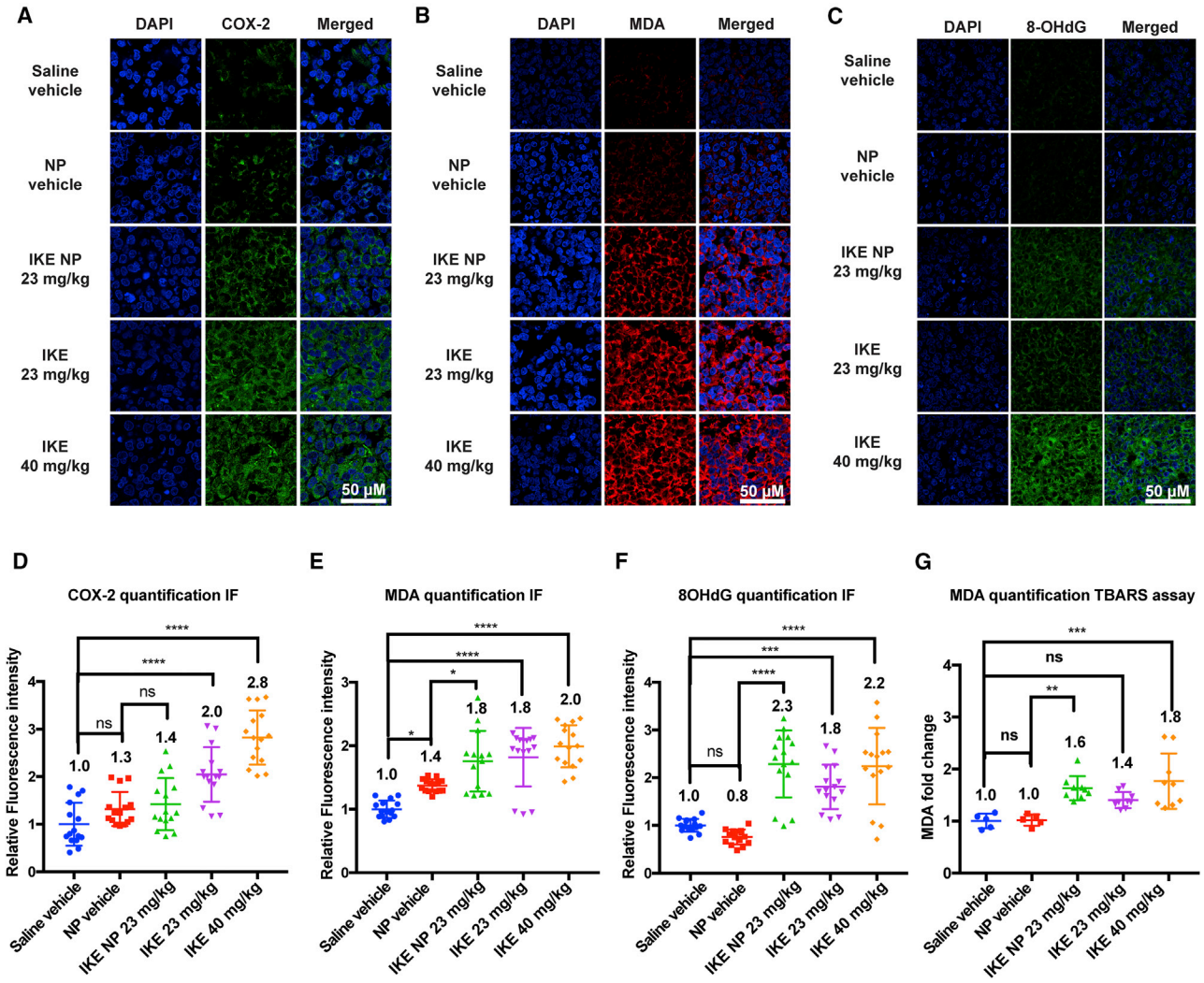

Figure 5. IKE Treatment Induced Lipid Peroxidation in Tumor Tissue during the Efficacy Study

(A and D) (A) Immunofluorescence and (D) quantification of COX-2 on frozen tumor sections showed 2.0- and 2.8-fold increase in COX-2 intensity upon IKE 23 mg/kg and IKE 40 mg/kg treatment daily for 14 days.

(B and E) (B) Immunofluorescence and (E) quantification of MDA on frozen tumor sections measured by confocal microscopy showed 1.4-, 1.8-, 1.8-, and 2.0-fold increase in MDA intensity upon NP vehicle, IKE NP 23 mg/kg, IKE 23 mg/kg, and IKE 40 mg/kg treatment daily for 14 days.

(C and F) (C) Immunofluorescence and (F) quantification of 8-OHdG on frozen tumor sections measured by confocal microscopy showed 2.3-, 1.8-, and 2.2-fold increase in 8-OHdG intensity upon IKE NP 23 mg/kg, IKE 23 mg/kg, and IKE 40 mg/kg treatment daily for 14 days. (Sections were cut from five randomly chosen mice in each group, three images from each section were captured on a Zeiss LSM 800 63×/1.40 oil DIC objective.)

(G) TBARS assay measuring MDA-TBA adduct fluorescence showed 1.6-, 1.4-, and 1.8-fold MDA increase upon IKE NP 23 mg/kg, IKE 23 mg/kg, and IKE 40 mg/kg treatment. ns, $p > 0.5$, *$p < 0.05$, **$p < 0.01$, ***$p < 0.001$, ****$p < 0.0001$ by one-way ANOVA. Data are plotted as the mean ± SD.

decreases or TAG decreases, indicating that Fenton chemistry-mediated lipid peroxidation is not likely a driver of most lipidomic changes during IKE-induced ferroptosis. Second, both the *de novo* and the remodeling pathways of phospholipids and TAG biosynthesis (Shindou and Shimizu, 2009) were activated following IKE treatment. Finally, lipidomic changes following induction of ferroptosis *in vivo* were characterized here. The data from the tumor samples revealed that DAGs, MAGs, and phospholipids were all significantly increased upon IKE treatment, possibly resulting from the activation of the TAG hydrolysis enzyme, ATGL, and the response of tumor cells to oxidative stress.

In addition, pharmacodynamic markers developed in this study may be beneficial for future ferroptosis efficacy studies. First, the qRT-PCR experiments identified a time-dependent up-regulation of numerous genes, including *PTGS2*, *SLC7A11*, and *CHAC1*, following IKE treatment in SUDHL6 cells and in xenograft tumor tissues derived from the same cell line. Second, immunofluorescence experiments showed increased levels of the *PTGS2* gene product COX-2, 8-OHdG, and dihydropyridine-MDA-lysine adducts in IKE-treated and IKE PEG-PLGA NP-treated tumors compared with vehicle, with no increased caspase-3 cleavage, a biomarker of apoptosis, in IKE-treated and IKE PEG-PLGA NP-treated tumor tissues. These data

collectively suggest that the antitumor effects of IKE result from system x_c^- inhibition-induced ferroptosis, but not apoptosis.

DLBCL cell lines have differential sensitivity to IKE-induced ferroptosis. The intrinsic factors determining DLBCL ferroptosis sensitivity remain to be explored to increase the understanding of ferroptosis and to enable selection of patients with sensitive tumors. The efficacy of IKE in additional animal cancer models would also be valuable to explore. Moreover, further studies on genes encoding lipid metabolism enzymes identified here would be useful to determine the essentiality of these genes for ferroptosis execution and the contribution of their expression to cell sensitivity to ferroptosis. In summary, we have developed a suitable small molecule and formulation for inhibiting system x_c^- and inducing ferroptosis in mouse tumor models and identified a series of pharmacodynamic markers of ferroptosis. These tools may be beneficial in determining whether there are specific cancer contexts in which ferroptosis induction would be therapeutically beneficial. The lipidomic study performed here may increase our understanding of the roles of lipids in ferroptotic cell death.

SIGNIFICANCE

Emerging evidence has shown the potential antitumor effects of using system x_c^- inhibitors and ferroptosis inducers as single reagents or in combination with chemotherapy in cell culture and some types of xenografts. It is thus important to identify biomarkers and understand the molecular mechanisms of ferroptosis inducers in both tumor cells and cancer models. Here we identify and establish the pharmacokinetic and pharmacodynamic properties of the ferroptosis inducer IKE in a xenograft model, which will be useful for future study of the therapeutic impact of ferroptosis in cancers and other conditions. The work presented here also identified a set of genes that are upregulated by IKE treatment in cell culture and demonstrated that the upregulation of these genes is due to system x_c^- inhibition, as illuminated following co-treatment with ferroptosis inhibitors. The integration of small-molecule tools, untargeted lipidomics, and qRT-PCR provides an efficient means to explore changes in lipid composition and lipid metabolic mechanisms during regulated cell death. Moreover, nanoparticle carriers provide an effective way to improve drug efficacy and reduce systemic toxicity because of targeted localization in tumors. Despite the various nanocarrier systems available and numerous advantages of nanoparticle therapeutics, there are challenges to applying nanocarriers *in vivo*. One such challenge is to manufacture uniform nanoparticles with high loading capacity at large scale. We utilized a scalable microfluidic platform, which allows for the precise engineering of PEG-PLGA nanoparticles. Given the rapid optimization process and the commercial availability of PEG-PLGA polymers, the nanoparticle system we used here may be useful to other researchers exploring *in vivo* delivery of ferroptosis inducers.

STAR★METHODS

Detailed methods are provided in the online version of this paper and include the following:

SUPPLEMENTAL INFORMATION

Supplemental Information includes five figures and two tables and can be found with this article online at https://doi.org/10.1016/j.chembiol.2019.01.008.

ACKNOWLEDGMENTS

We thank Dr. Brandon Fowler of Columbia University for assistance with mass spectrometry for IKE measurement and Hanqing Xiong of Columbia University for assistance with immunofluorescence and pharmacokinetics analysis. This research was supported by the National Cancer Institute (R35CA209896 and P01CA087497 to B.R.S).

AUTHOR CONTRIBUTIONS

Conceptualization, Y.Z. and B.R.S.; Methodology, Y.Z. and B.R.S.; Nanoparticle formulation design, cell line sensitivity test, and *in vitro* biochemical assays, B.R.S., Y.Z., and H.T.; Xenograft study and pharmacokinetics design, data collection, and analysis, B.R.S., Y.Z., J.D.D., and H.T.; Pharmacodynamic design and analysis, B.R.S. and Y.Z.; Immunofluorescence design and analysis, B.R.S., Y.Z., and H.L.; Untargeted lipidomic study design, data collection, and analysis, B.R.S., F.Z., and Y.Z.; Mouse mAb 1F83 provided by K.U.; some DLBCL cell lines provided by O.A.O.; Instrument access and support provided by L.M.B. for lipidomics., Writing – original draft, Y.Z. and B.R.S.; Writing – review & editing, Y.Z., H.L., J.D.D., F.Z., H.T., K.U., O.A.O., and B.R.S.; Supervision, B.R.S.; Funding acquisition, B.R.S.

DECLARATION OF INTERESTS

B.R.S. holds equity in and consults with Inzen Therapeutics. B.R.S. is an inventor on a patent related to this work. B.R.S. and Y.Z. are inventors on a patent application related to this work.

Received: October 8, 2018
Revised: November 19, 2018
Accepted: January 14, 2019
Published: February 21, 2019

REFERENCES

Blanco, E., Shen, H., and Ferrari, M. (2015). Principles of nanoparticle design for overcoming biological barriers to drug delivery. Nat. Biotechnol. *33*, 941.

Chakraborti, S. (2003). Phospholipase A2 isoforms: a perspective. Cell Signal. *15*, 637–665.

Chapuy, B., Stewart, C., Dunford, A.J., Kim, J., Kamburov, A., Redd, R.A., Lawrence, M.S., Roemer, M.G.M., Li, A.J., Ziepert, M., et al. (2018).

Molecular subtypes of diffuse large B cell lymphoma are associated with distinct pathogenic mechanisms and outcomes. Nat. Med. *24*, 679–690.

Chen, L., Li, X., Liu, L., Yu, B., Xue, Y., and Liu, Y. (2015). Erastin sensitizes glioblastoma cells to temozolomide by restraining xCT and cystathionine-γ-lyase function. Oncol. Rep. *33*, 1465–1474.

Dixon, S.J., Lemberg, K.M., Lamprecht, M.R., Skouta, R., Zaitsev, E.M., Gleason, C.E., Patel, D.N., Bauer, A.J., Cantley, A.M., and Yang, W.S. (2012). Ferroptosis: an iron-dependent form of nonapoptotic cell death. Cell *149*, 1060–1072.

Dixon, S.J., Patel, D.N., Welsch, M., Skouta, R., Lee, E.D., Hayano, M., Thomas, A.G., Gleason, C.E., Tatonetti, N.P., and Slusher, B.S. (2014). Pharmacological inhibition of cystine–glutamate exchange induces endoplasmic reticulum stress and ferroptosis. Elife *3*, e02523.

Doll, S., Proneth, B., Tyurina, Y.Y., Panzilius, E., Kobayashi, S., Ingold, I., Irmler, M., Beckers, J., Aichler, M., Walch, A., et al. (2017). ACSL4 dictates ferroptosis sensitivity by shaping cellular lipid composition. Nat. Chem. Biol. *13*, 91–98.

Gaschler, M.M., and Stockwell, B.R. (2017). Lipid peroxidation in cell death. Biochem. Biophys. Res. Commun. *482*, 419–425.

Gdowski, A., Johnson, K., Shah, S., Gryczynski, I., Vishwanatha, J., and Ranjan, A. (2018). Optimization and scale up of microfluidic nanolipomer production method for preclinical and potential clinical trials. J. Nanobiotechnol. *16*, 12.

Goracci, L., Tortorella, S., Tiberi, P., Pellegrino, R.M., Di Veroli, A., Valeri, A., and Cruciani, G. (2017). Lipostar, a comprehensive platform-neutral cheminformatics tool for lipidomics. Anal. Chem. *89*, 6257–6264.

Gout, P., Buckley, A., Simms, C., and Bruchovsky, N. (2001). Sulfasalazine, a potent suppressor of lymphoma growth by inhibition of the x c^- cystine transporter: a new action for an old drug. Leukemia *15*, 1633.

Guan, J., Lo, M., Dockery, P., Mahon, S., Karp, C.M., Buckley, A.R., Lam, S., Gout, P.W., and Wang, Y.-Z. (2009). The x c^- cystine/glutamate antiporter as a potential therapeutic target for small-cell lung cancer: use of sulfasalazine. Cancer Chemother. Pharmacol. *64*, 463.

Kagan, V.E., Mao, G., Qu, F., Angeli, J.P.F., Doll, S., St Croix, C., Dar, H.H., Liu, B., Tyurin, V.A., and Ritov, V.B. (2017). Oxidized arachidonic and adrenic PEs navigate cells to ferroptosis. Nat. Chem. Biol. *13*, 81.

Kim, S.E., Zhang, L., Ma, K., Riegman, M., Chen, F., Ingold, I., Conrad, M., Turker, M.Z., Gao, M., and Jiang, X. (2016). Ultrasmall nanoparticles induce ferroptosis in nutrient-deprived cancer cells and suppress tumour growth. Nat. Nanotechnol. *11*, 977–985.

Larraufie, M.-H., Yang, W.S., Jiang, E., Thomas, A.G., Slusher, B.S., and Stockwell, B.R. (2015). Incorporation of metabolically stable ketones into a small molecule probe to increase potency and water solubility. Bioorg. Med. Chem. Lett. *25*, 4787–4792.

Listenberger, L.L., Han, X.L., Lewis, S.E., Cases, S., Farese, R.V., Ory, D.S., and Schaffer, J.E. (2003). Triglyceride accumulation protects against fatty acid-induced lipotoxicity. Proc. Natl. Acad. Sci. U S A *100*, 3077–3082.

Liu, D.S., Duong, C.P., Haupt, S., Montgomery, K.G., House, C.M., Azar, W.J., Pearson, H.B., Fisher, O.M., Read, M., and Guerra, G.R. (2017). Inhibiting the system xC(-)/glutathione axis selectively targets cancers with mutant-p53 accumulation. Nat. Commun. *8*, 14844.

Lo, M., Ling, V., Low, C., Wang, Y., and Gout, P. (2010). Potential use of the anti-inflammatory drug, sulfasalazine, for targeted therapy of pancreatic cancer. Curr. Oncol. *17*, 9.

Lu, B., Chen, X.B., Ying, M.D., He, Q.J., Cao, J., and Yang, B. (2018). The role of ferroptosis in cancer development and treatment response. Front. Pharmacol. *8*, 992.

Magtanong, L., Ko, P.J., and Dixon, S.J. (2016). Emerging roles for lipids in non-apoptotic cell death. Cell Death Differ. *23*, 1099–1109.

McCullagh, E.A., and Featherstone, D.E. (2014). Behavioral characterization of system xc- mutant mice. Behav. Brain Res. *265*, 1–11.

Narang, V.S., Pauletti, G.M., Gout, P.W., Buckley, D.J., and Buckley, A.R. (2007). Sulfasalazine-induced reduction of glutathione levels in breast cancer cells: enhancement of growth-inhibitory activity of doxorubicin. Chemotherapy *53*, 210–217.

Sato, H., Shiiya, A., Kimata, M., Maebara, K., Tamba, M., Sakakura, Y., Makino, N., Sugiyama, F., Yagami, K., Moriguchi, T., et al. (2005). Redox imbalance in cystine/glutamate transporter-deficient mice. J. Biol. Chem. *280*, 37423–37429.

Sato, M., Kusumi, R., Hamashima, S., Kobayashi, S., Sasaki, S., Komiyama, Y., Izumikawa, T., Conrad, M., Bannai, S., and Sato, H. (2018). The ferroptosis inducer erastin irreversibly inhibits system xc^- and synergizes with cisplatin to increase cisplatin's cytotoxicity in cancer cells. Sci. Rep. *8*, 968.

Sengupta, A., Lichti, U.F., Carlson, B.A., Cataisson, C., Ryscavage, A.O., Mikulec, C., Conrad, M., Fischer, S.M., Hatfield, D.L., and Yuspa, S.H. (2013). Targeted disruption of glutathione peroxidase 4 in mouse skin epithelial cells impairs postnatal hair follicle morphogenesis that is partially rescued through inhibition of COX-2. J. Invest. Dermatol. *133*, 1731–1741.

Shindou, H., and Shimizu, T. (2009). Acyl-CoA: lysophospholipid acyltransferases. J. Biol. Chem. *284*, 1–5.

Skouta, R., Dixon, S.J., Wang, J., Dunn, D.E., Orman, M., Shimada, K., Rosenberg, P.A., Lo, D.C., Weinberg, J.M., and Linkermann, A. (2014). Ferrostatins inhibit oxidative lipid damage and cell death in diverse disease models. J. Am. Chem. Soc. *136*, 4551–4556.

Stockwell, B.R., Angeli, J.P.F., Bayir, H., Bush, A.I., Conrad, M., Dixon, S.J., Fulda, S., Gascón, S., Hatzios, S.K., and Kagan, V.E. (2017). Ferroptosis: a regulated cell death nexus linking metabolism, redox biology, and disease. Cell *171*, 273–285.

Sun, T., Zhang, Y.S., Pang, B., Hyun, D.C., Yang, M., and Xia, Y. (2014). Engineered nanoparticles for drug delivery in cancer therapy. Angew. Chem. Int. Ed. *53*, 12320–12364.

Uchida, K. (2017). HNE as an inducer of COX-2. Free Radic. Biol. Med. *111*, 169–172.

Valencia, P.M., Pridgen, E.M., Rhee, M., Langer, R., Farokhzad, O.C., and Karnik, R. (2013). Microfluidic platform for combinatorial synthesis and optimization of targeted nanoparticles for cancer therapy. ACS Nano *7*, 10671–10680.

Yamada, S., Kumazawa, S., Ishii, T., Nakayama, T., Itakura, K., Shibata, N., Kobayashi, M., Sakai, K., Osawa, T., and Uchida, K. (2001). Immunochemical detection of a lipofuscin-like fluorophore derived from malondialdehyde and lysine. J. Lipid Res. *42*, 1187–1196.

Yamaguchi, H., Hsu, J.L., Chen, C.-T., Wang, Y.-N., Hsu, M.-C., Chang, S.-S., Du, Y., Ko, H.-W., Herbst, R., and Hung, M.-C. (2013). Caspase-independent cell death is involved in the negative effect of EGF receptor inhibitors on cisplatin in non–small cell lung cancer cells. Clin. Cancer Res. *19*, 845–854.

Yang, W.S., Kim, K.J., Gaschler, M.M., Patel, M., Shchepinov, M.S., and Stockwell, B.R. (2016). Peroxidation of polyunsaturated fatty acids by lipoxygenases drives ferroptosis. Proc. Natl. Acad. Sci. U S A *113*, E4966–E4975.

Yang, W.S., Sriramaratnam, R., Welsch, M.E., Shimada, K., Skouta, R., Viswanathan, V.S., Cheah, J.H., Clemons, P.A., Shamji, A.F., and Clish, C.B. (2014). Regulation of ferroptotic cancer cell death by GPX4. Cell *156*, 317–331.

Yu, H.T., Guo, P.Y., Xie, X.Z., Wang, Y., and Chen, G. (2017). Ferroptosis, a new form of cell death, and its relationships with tumourous diseases. J. Cell Mol. Med. *21*, 648–657.

Yu, Y., Xie, Y., Cao, L., Yang, L., Yang, M., Lotze, M.T., Zeh, H.J., Kang, R., and Tang, D. (2015). The ferroptosis inducer erastin enhances sensitivity of acute myeloid leukemia cells to chemotherapeutic agents. Mol. Cell. Oncol. *2*, e1054549.

Yue, Z., You, Z., Yang, Q., Lv, P., Yue, H., Wang, B., Ni, D., Su, Z., Wei, W., and Ma, G. (2013). Molecular structure matters: PEG-b-PLA nanoparticles with hydrophilicity and deformability demonstrate their advantages for high-performance delivery of anti-cancer drugs. J. Mater. Chem. B *1*, 3239–3247.

Zilka, O., Shah, R., Li, B., Friedmann Angeli, J.P., Griesser, M., Conrad, M., and Pratt, D.A. (2017). On the mechanism of cytoprotection by ferrostatin-1 and liproxstatin-1 and the role of lipid peroxidation in ferroptotic cell death. ACS Cent. Sci. *3*, 232–243.

STAR★METHODS

KEY RESOURCES TABLE

REAGENT or RESOURCE	SOURCE	IDENTIFIER
Antibodies		
Anti-dihydropyridine-MDA-lysine adduct mouse mAb 1F83	Reference (Yamada et al., 2001)	N/A
Anti-8-OH-dG antibody	Abcam	Cat# ab62623; RRID: AB_940049
Anti-xCT antibody	Abcam	Cat# ab37185; RRID: AB_778944
Anti-cyclooxygenase 2 (COX-2) antibody	Abcam	Cat# ab15191; RRID: AB_2085144
Goat anti-mouse IgG H&L (Alexa Fluor 647)	Abcam	Cat# ab150115; RRID: AB_2687948
Goat anti-rabbit IgG H&L highly cross-adsorbed secondary antibody (Alexa Fluor488)	Thermo Fisher Scientific	Cat# A11034; RRID: AB_2576217
Donkey anti-Goat IgG (H+L) cross-adsorbed, Alexa Fluor 647, polyclonal, secondary antibody	Thermo Fisher Scientific	Cat# A21447; RRID: AB_141844
Anti-α-tubulin antibody (DM1A)	Santa Cruz Biotechnology	sc-32293
Anti-xCT/SLC7A11 (D2M7A) antibody	Cell Signaling Technology	12691
Anti-caspase-3 antibody	Cell Signaling Technology	9662
Chemicals, Peptides, and Recombinant Proteins		
(Poly(ethylene glycol) methyl ether-*block*-poly(lactide-*co*-glycolide) (PEG-PLGA)	Sigma-Aldrich	900948
β-mercaptoethanol	Sigma-Aldrich	M3148
Imidazole ketone erastin (IKE)	Reference(Larraufie et al., 2015)	N/A
Ferrostatin-1 (fer-1)	Reference(Skouta et al., 2014)	N/A
Critical Commercial Assays		
GSH/GSSG Ratio Detection Assay Kit	Abcam	ab13881
TBARS Assay Kit	Cayman	700870
BODIPY™ 581/591 C11	Thermo Fisher Scientific	D3861
RiboPure™ RNA Purification Kit	Thermo Fisher Scientific	AM1924
CellTiter-Glo Luminescent Cell Viability Assay	Promega	G7573
RNAeasy extraction kit	QIAGEN	74106
QIAshredder	QIAGEN	79656
High Capacity cDNA Reverse Transcription Kit	Thermo Fisher Scientific	4368814
Power SYBR Green PCR Master Mix	Thermo Fisher Scientific	4368702
Other		
ProLong™ Gold anti-fade Mount with DAPI	Thermo Fisher Scientific	P36962
10% goat serum	Thermo Fisher Scientific	50197Z
Donkey serum	Sigma-Alderich	D9663
Poly-lysine	Sigma-Aldrich	P4832
Fetal bovine serum	Thermo Fisher Scientific	10437-028
DMEM	Corning	10-013
Fetal bovine serum	Life Technologies	10437036
RPMI-1640	ATCC	30-2001
Non-essential amino acids	Thermo Fisher Scientific	11140076
Penicillin-streptomycin mix	Thermo Fisher Scientific	15140148
IMDM	Thermo Fisher Scientific	12440053
HBSS	Thermo Fisher Scientific	14025076
Steriflip filter unit	Thomas Scientific	1189Q46
Amicon Ultra-15 centrifugal filter units	Millipore	UF9050
K3 EDTA micro tube	SARSTEDT	41.1504.105

(*Continued on next page*)

Continued

REAGENT or RESOURCE	SOURCE	IDENTIFIER
RIPA buffer	Thomas Scientific	89900
Software and Algorithms		
ChemDraw Ultra, Version 14.0	Perkin Elmer	http://www.perkinelmer.com/category/chemdraw
Prism, Version 7.0	GraphPad Software	https://www.graphpad.com/scientific-software/prism/
LipoStar, Version 1.0.4	Molecular Discovery	https://www.moldiscovery.com/software/lipostar/
MetaboAnalyst, Version 4.0	MetaboAnalyst	https://www.metaboanalyst.ca/faces/docs/About.xhtml
MassLynx, Version 4.1	Waters	http://www.waters.com/waters/en_US/MassLynx-Mass-Spectrometry-Software-/nav.htm?cid=513164&locale=en_US
XCMS package, Version 3.2.0	Bioconductor	http://packages.renjin.org/package/org.renjin.bioconductor/xcms

CONTACT FOR REAGENTS AND RESOURCES SHARING

Further information and requests for resources and reagents should be directed to and will be fulfilled by the Lead Contact Brent R. Stockwell (bstockwell@columbia.edu).

EXPERIMENTAL MODEL AND SUBJECT DETAILS

Cell lines and cell culture information is listed below. The SUDHL-5 (female), SUDHL-6 (male), SUDHL-16 (male), and HT-1080 (male) cell lines were obtained from ATCC. The DOHH-2 (male) cell line was obtained from DSMZ. The HBL-1 (male), U2932 (female), SUDHL-7 (male), SUDHL-9 (male), A4/FUK (female), WSU-NHL (female), Ly18 (OCI-Ly18) (male), Karpas422 (female), SUDHL-1 (male), SUDHL-2 (female), SUDHL-8 (male), SUDHL-10 (male), A3/KAW (female), RIVA (female), Ly9 (OCI-Ly9) (male), U937 (male), and Ly7 (OCI-Ly7) (male) cell lines were provided by Dr. Owen A. O'Connor (Columbia University) and the Columbia Genome Center. HT-1080 cells were grown in DMEM with glutamine and sodium pyruvate (Corning 10-013) supplemented with 10% heat-inactivated fetal bovine serum (FBS) (Life Technologies, 10437036) 1% non-essential amino acids (Thermo Fisher Scientific, 11140076) and 1% penicillin-streptomycin mix (pen-strep) (Thermo Fisher Scientific, 15140148). SUDHL-1, SUDHL-2, SUDHL-6, SUDHL-8, SUDHL-10, SUDHL-16, A3/KAW, RIVA, Ly8 and U937 cells were cultured in RPMI-1640 (ATCC 30-2001) with 10% FBS and 1% pen-strep. DOHH-2, HBL-1, U2932, SUDHL-7, SUDHL-9, A4/FUK, WSU-NHL, and Ly8 were cultured in RPMI-1640 with 10% heat-inactivated FBS and 1% pen-strep. SUDHL-5 and Karpas422 were cultured in RPMI-1640 with 20% FBS and 1% pen-strep. Ly7 was cultured in IMDM (Thermo Fisher Scientific, 12440053) with 15% heat-inactivated FBS and 1% pen-strep. All cells were maintained in a humidified environment at 37°C and 5% CO_2 in an incubator.

The animal models used in the paper is listed below. The animal studies reported in this manuscript adhere to the ARRIVE guidelines. All animal study protocols were approved by the Columbia University Institutional Animal Care and Use Committee (IACUC). NOD-*Prkdc*^{em26Cd52}*Il2rg*^{em26Cd22}/NjuCrl (NCG) mice (Charles River, strain code 572) (male, 5-weeks of age) and NOD.CB17-*Prkdcscid*/*J* (NOD SCID) mice (The Jackson Laboratory, stock number 001303) (male, 5-weeks of age)) were acclimated after shipping for >3 days before beginning experiments. Mice were fed a standard diet (PicoLab 5053) and maintained with no more than 5 mice per cage.

METHODS DETAILS

Animal Studies

Pharmacokinetic Analysis in Mice with Three Different Administration Routes

NOD/SCID mice (12-weeks of age and ~28 g weight) were weighed before injection and divided into groups of 3 mice per cage. IKE was dissolved in 5% DMSO/95% Hank's Balanced Salt Solution (HBSS) (Thermo Fisher Scientific, 14025076), pH 4, to create a 5 mg/mL solution. 5% DMSO/95% HBSS at pH 4 solution (Vehicle 1) without IKE was used as vehicle. The solution was sterilized using a 0.22 μm Steriflip filter unit (Thomas Scientific 1189Q46). Mice were dosed using three different routes, IP and PO with 50 mg/kg IKE, and IV with 17 mg/kg IKE. Samples were collected at 0, 1, 3, 4, and 8 h from three mice per time point. Additionally, three mice per group were used as controls by administration with equivalent amount of vehicle 1 by IP, PO, and IV, and samples were collected at 8 h. At the appropriate time, mice were sacrificed by CO_2 asphyxiation for 3 min and ~0.5 mL of blood was collected via cardiac puncture. Blood was immediately put into K3 EDTA micro tube (SARSTEDT 41.1504.105) and placed on ice. Samples were centrifuged for 10 min at 2,100 x *g* at 4°C, then plasma was transferred to a clean tube. Plasma samples were flash frozen in liquid nitrogen and stored at -80°C. IKE was extracted from plasma by adding 900 μL acetonitrile to 100 μL plasma. Samples were mixed for at least 5 min by rotating at room temperature and were sonicated prior to concentration for 10 min at 4,000 x *g* and 4°C. The

supernatant was removed and dried on a GeneVac evaporator overnight on an HPLC setting. After drying, the samples were re-suspended in 100 μL of methanol and analyzed on the liquid chromatography mass spectrometry (LC-MS), with each sample analyzed twice. Quality control standard samples were prepared by dissolving IKE in 100 μL water and extraction with the same procedures to ensure that the extraction was efficient. LC-MS analysis was performed on a platform comprising a Thermo Scientific Dionex Ultimate 3000RS controlled by Chromeleon (Dionex) and a Bruker amazon SL ESI ion-trap mass spectrometer.

Chromatographic separation was performed at 20°C on Agilent Eclipse Plus C18 column (2.1 x 50 mm, 3.5 μm) at 20°C over a 12 minute gradient elution. Mobile phase A consisted of water with 0.1% acetic acid v/v and mobile phase B was methanol with 0.1% acetic acid v/v. After injection, the gradient was held at 80% mobile phase A for 1 min. The gradient was then ramped in a linear fashion to 80% mobile phase over 0.5 min. Over the next 3.5 min, the gradient was ramped in linear fashion to 100% mobile phase B and held at 100% mobile phase B for 3.25 min. The gradient was then ramped in a linear fashion to 80% mobile phase over 0.5 min and held there for the duration of the run. The flow rate was set to 400 μL/min and injection volumes were 5 μL. The retention time for IKE in this gradient was 2.8 min.

Mass spectrometry analysis was performed on a Bruker Amazon SL (Billerca, MA) in positive ESI mode. Trap Control was used to control the ESI settings with the inlet capillary held at -4500 V and the end plate offset at -500 V. Nitrogen was used as the desolvation gas. Hystar v3.2 was used to integrate the UHPLC and MS applications, and data analysis was performed with the Compass DataAnalysis software. The base peak chromatogram at m/z 655.2 with a width of ± 0.1 was integrated and peak area quantified by standard curve.

Pharmacokinetics (PK) of IKE were assessed using Prism fitted with lognormal of one phase exponential decay. The PK parameters are summarized in Table S1.

Pharmacokinetic and Pharmacodynamic Analysis in NCG Mice Bearing SUDHL6 Xenografts

IKE was dissolved in 5% DMSO/95% HBSS at pH 4 to create a 5 mg/mL solution or 3 mg/mL solution. 5% DMSO/95% HBSS at pH 4 was used as vehicle 1. IKE PEG-PLGA nanoparticles and unfunctionalized PEG-PLGA nanoparticles (without IKE) (vehicle 2) prepared with a NanoAssemblr were dialyzed with deionized water overnight, and the water was changed at least twice. Dialyzed IKE-PEG-PLGA nanoparticles and unfunctionalized PEG-PLGA nanoparticles were concentrated by Amicon Ultra-15 Centrifugal Filter Units to create a solution with 80 mg/mL PEG-PLGA nanoparticles. All above solutions were sterilized by filtering through a 0.2 μm syringe filter.

NCG mice 6 weeks of age were injected with 10 million SUDHL-6 cells subcutaneously. Visible tumors appeared after 2 weeks. Tumor size was measured by electronic caliper every 2 days and calculated using the formula: 0.5 x length x width^2. After another 2 weeks, mice were randomly separated into group of 3 mice per cage with roughly tumor size (1,200 mm^3). Mice were dosed at 50 mg/kg IKE using IP at one time and samples were collected at 0, 1, 2, 3, 4, 6, and 24 h with three mice per time point. Mice were dosed with DMSO vehicle by IP and samples were collected at 24 h. Mice were euthanized using a CO_2 gas chamber before xenograft dissection and cardio puncture. Plasma samples were collected and analyzed as described above. Tumors were dissected and divided into 6 segments, frozen on dry ice, and stored at -80°C. Before IKE extraction, tumor tissue samples were thawed at room temperature and weighed. A 2.5-fold ratio of volume of phosphate-buffered saline (PBS) (mL/g) was added to the sample and homogenized using Bead Ruptor 4 at speed 4 for 30 sec. The homogenization step was repeated until the samples were homogenized well (final weight/volume was 0.4 g/mL). 100 μL of homogenized tissue (equal to 40 mg) was added to a new microfuge tube, 900 μL of acetonitrile was added. The samples were mixed for at least 5 minutes by rotating on a shaker and were sonicated for at least 30 sec prior to centrifugation for 10 min at 4,000 x *g* and 4°C. The supernatant was removed and dried on the GeneVac overnight on the HPLC setting. After drying, the samples were resuspended in 100 μL of methanol and analyzed on the LC-MS with each sample analyzed twice. Technical replicates were averaged. The concentration of IKE in the sample was determined by comparison against a standard curve of IKE in the range of 25 to 2,500 ng/mL. Pharmacodynamic analysis of ferroptosis biomarkers is described in the RT-qPCR, glutathione, immunofluorescence, and lipidomics sections below. Pharmacokinetics parameters of IKE was assessed using Prism fitted with Lognormal of one phase exponential decay. The PK parameters are summarized in Table S2.

IKE Efficacy Study

IKE was dissolved in 5% DMSO/95% HBSS at pH 4 to create a 4 mg/mL solution. 5% DMSO/95% HBSS at pH 4 was used as vehicle 1. IKE PEG-PLGA nanoparticles and unfunctionalized PEG-PLGA nanoparticles (without IKE loading) (vehicle 2) prepared with a NanoAssemblr were dialyzed with deionized water overnight; the water was changed at least twice. Dialyzed IKE-PEG-PLGA nanoparticles and unfunctionalized PEG-PLGA nanoparticles were concentrated by Amicon Ultra-15 Centrifugal Filter Units to create a solution with 80 mg/mL PEG-PLGA nanoparticles. All above solutions were sterilized by filter through a 0.2 μm syringe filter.

NCG mice, 6-weeks old, were injected with 10 million SUDHL0-6 cells subcutaneously. The mice were treated after the tumor size reached 100 mm^3. Mice were separated randomly into treatment groups and dosed with 23 mg/kg IKE, 40 mg/kg IKE, 23 mg/kg IKE PEG-PLGA nanoparticles (equal to 700 mg/kg PEG-PLGA), vehicle 1 (based on volume), and vehicle 2 (700 mg/kg PEG-PLGA) once daily by IP for 14 days. Tumor volume was measured daily with electronic caliper and calculated using the formula: 0.5 x length x width^2. 3 h after the final dosage, mice were euthanized with CO_2 and tumor tissue was dissected, weighed, divided into 4-6 segments, frozen, and stored at -80°C. Tumor volume change was analyzed in Prism using one-way ANOVA. IKE accumulation in tumor tissues were analyzed using the same method in the above sections. Biomarker characterization in tumor tissues were described in the RT-qPCR, immunofluorescence, TBARS, and lipidomics sections below.

DLBCL Lines Sensitivity Measurement

DLBCL cells were plated at 10,000 cells per well in white 384-well plates (32 μL per well) in technical duplicates and incubated overnight. The cells were then treated with 8 μL medium containing a two-fold dilution series of vehicle (DMSO), IKE (starting from 100 μM) with or without Fer-1 (starting from 200 μM). After 24 h incubation, 40 μL of 50% CellTiter-Glo (Promega) 50% cell culture medium was added to each well and incubated at room temperature with shaking for 15 min. Luminescence was measured using a Victor X5 plate reader (PerkinElmer). All cell viability data were normalized to the DMSO vehicle condition. Experiments were performed three independent times with different passages for each cell line. From these data, dose-response curves and IC_{50} values were computed using Prism 7.0 (GraphPad).

Flow Cytometry Assay

0.20 million SUDHL-6 cells were seeded in six-well plates and treated with DMSO, IKE, or fer-1 at specific concentration. The final cell density was 0.05 million cells/mL. After 24 h, cells were harvested by centrifuging at 300 x *g* for 5 min. Cells were resuspended in 500 μL HBSS containing 2 μM C11-BODIPY (BODIPY 581/591 C11) (Thermo Fisher Scientific, D3861) and incubated at 37°C for 15 min. Cells were pelleted and resuspended in HBSS. Fluorescence intensity was measured on the FL1 channel with gating to record live cells only (gate constructed from DMSO treatment group). A minimum of 10,000 cells were analyzed per condition.

Reduced Glutathione Measurement

2.4 million cells were incubated with DMSO, IKE, or β-mercaptoethanol (β-ME) at a density of 0.2 million cells/mL for 24 h. Cells were collected and washed with cold PBS once. Cell number was counted by Vi-Cell. Cells were resuspended in ice-cold RIPA buffer (Thermo Fisher Scientific, 89900) with 100 μL/one million cells. Samples were centrifuged for 15 min at 4°C at 17,000 x *g*. The resulting supernatant was deproteinized using a trichloroacetic acid and sodium bicarbonate solution and kept on ice. The sample was diluted with assay buffer provided in GSH/GSSG Ratio Detection Assay Kit (Abcam, ab13881) ten-fold. Reduced glutathione (GSH) levels were determined using Fluorometric-Green provided in the kit following the manufacture's protocol. 384-well (Corning) low volume black flat bottom polystyrene non-treated microplates 1230F99 were used.

To perform reduced glutathione measurement in tumor tissue, 10 mg of tumor tissue was mixed with 400 μL RIPA buffer, homogenized at speed 5 for 30 sec using a Bead Ruptor 4 (OMNI International). The sample was centrifuged at 17,000 x *g* for 5 min, then the above deprotenization and measurement steps performed.

TBARS Assay

10-25 mg tumor tissue was placed into a 1.5 mL Eppendorf microfuge tube, and the sample was placed on dry ice until use. 20 μL/mg ice-cold RIPA buffer with cocktail protease inhibitor (Roche) was added. The tumor tissue was homogenized at speed 5 for 30 sec using Bead Ruptor 4. The sample was centrifuged at 4°C at 1,600 x *g* for 10 min. The sample was kept on ice and the supernatant used for analysis. Tissue homogenates did not need to be diluted before assaying. TBARS was measured using a TBARS Assay Kit (Cayman 700870), following the manufacture's protocol.

qPCR

To perform qPCR analysis in cell culture, DLBCL cells were treated with 0-10 μM IKE, fer-1, or β-ME for the indicated times. RNA was extracted using the Qiashredder and Qiagen RNeasy Mini kits (Qiagen) according to the manufacture's protocol. 2 μg RNA from each sample was reversed transcribed to cDNA using a High Capacity cDNA Reverse Transcription Kit (Thermo Fisher Scientific, 4368814). Quantitative PCR reactions were performed using Power SYBR Green PCR Master Mix (Applied Biosystems) with triplicate measurement on ViiA 7 Real-Time PCR instrument (Thermo Fischer). *HPRT1* was used as an internal reference. Differences in mRNA levels compared with *HPRT1* were computed between vehicle and experimental groups using the ΔΔCt method. The primers used in the study was listed below.

Genes	Foward	Reverse
HPRT1	5'-GCCCTGGCGTCGTGATTAGTG-3'	5'-GCCTCCCATCTCCTTCATCAC-3'
CHAC1	5'- GAACCCTGGTTACCTGGGC-3'	5'- CGCAGCAAGTATTCAAGGTTGT-3'
SLC7A11	5'-GGTGGTGTGTTTGCTGTC-3'	5'-GCTGGTAGAGGAGTGTGC-3'
PTGS2	5'- ATATGTTCTCCTGCCTACTGGAA-3'	5'-GCCCTTCACGTTATTGCAGATG-3'
ACSL4	5'-CCCCGCTATCT CTCAGACAC-3'	5'-GGTGCTCCAACTCTGCCAG-3'
FASN	5'-CTTCCGAGATTCCATCCTACGC-3'	5'-TGGCAGTCAGGCTCACAAACG-3'
ELOVL1	5′-TCCCTCTACATTGTCTATGAGTTCC-3′	5′-TTCAGTTGGCCTTGACCTTGGCAATACC-3'
ELOVL7	5′-AGGATCCATGGCCTTCAGTGATCTTACATCGAGG-3'	5′-AACCACCTGCAGCAAATTTGACTCC-3'
ALOX12	5'-AGAAAAGTTGACTAGTCCAGTGTGGTGAA-3'	5'-AAAAGCTGTGCTAAACCAATTCCGAACAGATTCTCA-3'
ALOX15	5'-GGAGCCTTCCTAACCTACAGC-3'	5'-CTCACGATTCCTTCCACATACC-3'

(*Continued on next page*)

Continued

Genes	Foward	Reverse
LPCAT1	5'-CACAACCAAGTGGAAATCGAG-3'	5'-GCACGTTGCTGGCATACA-3'
LPCAT3	5'-ATCACTGCCGTCCTCACTAC-3'	5'-AGTCAACAGCCAAACCAATC-3'
LPCAT4	5'-GGTGGGAGAGAATGCCACTT-3'	5'-ATGCAAGGGATGATGGCTGT-3'
LPEAT1	5'-CTGAAATGTGTGTGCTATGAGCG-3'	5'-TGGAAGAGAGGAAGTGGTGTCTG-3'
ACC1	5'-GAGGGCTAGGTCTTTCTGGAAG-3'	5'-CCACAGTGAAATCTCGTTGAGA-3'
sPLA2F	5'-TGACGACAGGAAAGGAAGCCGCAC-3'	5'-AGGGAAGAGGGGACTCAGCAACGAG-3'
PLA2G6C	5'-CTGGAACCTGTGTTGGACCT-3'	5'-CGGTGATATCTGTGGTCACG-3'
ATGL	5'-CAACGCCACTCACATCTACGG-3'	5'-GGACACCTCAATAATGTTGGCAC-3'

To perform qPCR analysis in mouse tumor tissue, ~20 mg of tumor tissue was prepared and kept on dry ice. The frozen tissue was homogenized with Bead Ruptor 4 at speed 4 for 30 sec. The homogenization was repeated once if there remained unhomogenized tissue. Total mRNA was prepared from the cleared homogenate using Ribopure Kit (Thermo Fisher Scientific, am1924). RNA was reverse transcribed to cDNA then used in quantitative PCR experiment following the same steps used in cell qPCR experiment.

Immunofluorescence Study and Quantification

Immunofluorescence Study and Quantification on Cells

SUDHL-6 cells were treated with IKE. The cells were harvested by centrifugation and washed with PBS once. The cells were resuspended in PBS, fixed by adding equal volume of 4% paraformaldehyde (PFA), and incubated at room temperature for 15 min. The cells were washed with PBS/0.1% Tween 20 (PBST) twice, resuspended in 10% goat serum (ThermoFisher 50197Z) for 1 h. The cells were incubated with mouse mAb 1F83, which specifically recognizes the malondialdehyde (MDA)-lysine adduct 4-methyl-1,4-dihydropyridine-3,5-dicarbaldehyde (MDHDC)(Yamada et al., 2001) (1:100 dilution) overnight at 4°C. The cells were washed with PBS three times by centrifugation. The cells were incubated with goat anti-mouse IgG H&L (Alexa Fluor 647) (Abcam ab150115) (1:1000) at room temperature for 1 h. The cells were washed with PBST twice by centrifugation, then resuspended in PBS in 24-well plate with poly-lysine-(Sigma Aldrich P4832)-coated cover slips and centrifuged at 1,000 x *g* for 10 min. ProLong Diamond antifade mountant with DAPI (ThermoFisher P36962) was added to stain the nucleus. All images were captured on a Zeiss LSM 800 confocal microscope at Plan-Apochromat 63x/1.40 Oil DIC objective with constant laser intensity for all samples. When applicable, line-scan analysis was performed on representative confocal microscopy images using Zeiss LSM software to qualitatively visualize fluorescence overlap. The intensity above threshold of the fluorescent signal of the bound antibodies was analyzed using NIH ImageJ software. Data were expressed as fold change compared with the vehicle.

Immunofluorescence Study and Quantification on Frozen Tissue Sections

Tumor tissues were fixed in 4% paraformaldehyde (PFA) for 24h at 4°C followed by washing with PBS three times. The tissues were perfused in 30% sucrose for 24h at 4°C for cryo-protection. The samples were embedded in OCT cryostat sectioning medium, and then moved directly into a cryostat. After equilibration of temperature, frozen tumor tissues were cut into 5 μm thick sections. Tissue sections were mounted on to poly-L-lysine coated slides by placing the cold sections onto warm slides. Slides were stored at -80°C until staining. For staining, slides were warmed to room temperature followed by washing with PBS twice. A hydrophobic barrier pen was used to draw a circle on each slide. The slides were permeabilized with PBS/0.4% Triton X-100 twice before non-specific-binding blocking by incubating the sections with 10% goat serum (ThermoFisher 50197Z) for 30 minutes at room temperature. The sections were separately incubated with mouse anti-MDA mAb 1F83 (1:1000 dilution), anti-cyclooxygenase 2 (COX 2, AKA PTGS2) antibody (Abcam, ab15191, 1:200 dilution), or anti-8-OH-dG (DNA/RNA damage) antibody (Abcam, ab62623, 1:200 dilution) overnight at 4°C in humidified chambers. Sections were washed with PBST for twice before incubating with goat anti-mouse IgG H&L (Alexa Fluor 647) (Abcam, ab150115, 1:1000 dilution) or goat anti-rabbit IgG H&L highly cross-absorbed secondary antibody (Alexa Fluor488, Thermo Fisher Scientific, A-11034, 1:1000) at room temperature for 1 h. Slides were then washed twice with PBST. ProLong Diamond antifade mountant with DAPI (ThermoFisher P36962) was added onto slides, which were then covered with the coverslips, sealed by clear fingernail polish and observed under confocal microscopy. All images were captured on a Zeiss LSM 800 confocal microscope at Plan-Apochromat 63x/1.40 Oil DIC objective with constant laser intensity for all analyzed samples. The intensity above threshold of the fluorescent signal of the bound antibodies was analyzed using NIH ImageJ software. Data were expressed as fold change comparing with the vehicle.

Immunofluorescence Study and Quantification on Paraffin-Embedded Tissue Sections

Tumor tissue was fixed in 4% paraformaldehyde (PFA) for 24 h at 4°C followed by washing three times with PBS. The samples were fixed in paraffin. Six series of 5 μM sections were obtained with a sliding microtome. The serial sections were then mounted on gelatin-coated slide. The paraffin-embedded tissue sections were deparaffinized with xylene three times, 5 min each, followed by rehydrating in 100%, 90%, 70%, and 50% ethanol, two washes 5 min each, then rinsed with distilled water. Antigen retrieval was performed in Tris-EDTA buffer, pH 9.0, 95-100°C for 10 min. Then sections were rinsed in PBST, 2 min each. Then the above steps were followed for staining and quantification.

Western Blot

10-25 mg tumor tissue was placed into a 1.5 mL Eppendorf microfuge tube, and the sample was placed on dry ice until use. 20 μL/mg ice cold RIPA buffer with cocktail protease inhibitor (Roche) was added. The tumor tissue was homogenized at speed 5 for 30 sec using Bead Ruptor 4. The sample was centrifuged at 4°C at 1,600 x *g* for 10 min. The sample was kept on ice and the supernatant used for analysis. Caspase-3 antibody which could recognize both full-length caspase-3 and cleaved caspae-3 was used. α-tubulin antibody was used as the reference.

Nanoparticle Formulation and Characterization

Formulation

(Poly(ethylene glycol) methyl ether-*block*-poly(lactide-*co*-glycolide) (PEG-PLGA) with PEG average M_n 5,000, PLGA M_n 15,000, and lactide:glycolide 50:50 was purchased from Sigma-Aldrich (900948). PEG-PLGA nanoparticles were prepared using a microfluidic mixer with the NanoAssemblr Benchtop instrument (Precision NanoSystems Inc., Vancouver, BC) by mixing oil and aqueous phases. PEG-PLGA was dissolved in 25% acetone/75% DMSO at concentration of 10 mg/mL. Milli-Q water was used as aqueous phase. For synthesis of PEG-PLGA nanoparticles, two phases were injected through two inlets of the microfluidic mixer with a speed of 8 mL/min and a volume ratio of 1:1. Nanoparticles were collected in the sample collection tube by discarding an initial and final waste volume of 0.25 and 0.05 mL. Samples were dialyzed in at least 500 x deionized water overnight using 10 kD cut-off dialysis bag (ThermoFisher, SnakeSkin Dialysis Tubulin, 68100) and the water was changed twice in between to remove organic solvent. Then the purified nanoparticles were concentrated by centrifuging using Amicon Ultra-15 Centrifugal Filter Units (Millipore, UF9050) at 2,168 x *g* to the desired concentration. For encapsulation of IKE, IKE was dissolved in a solution of PEG-PLGA in 25% acetone and 75% DMSO. The final concentration of PEG-PLGA was 10 mg/mL and IKE was 1.5 mg/mL. The process was the same with PEG-PLGA nanoparticles preparation. Nanoparticle size and potential were measured using a Malvern Zetasizer Nano ZS.

IKE Quantification in PEG-PLGA Nanoparticles

IKE concentration was determined in PEG-PLGA nanoparticles using Liquid Chromatography- Mass Spectrometry (LC -MS). IKE was extracted from nanoparticles by mixing 100 μL of samples with 900 μL of acetonitrile. After mixing for 1 h, the mixture was sonicated for 5 min and then centrifuged at 4000 rpm for 10 min. The supernatant was transferred to a new vial. The organic solvent was removed by Genevac evaporation. The residues were re-dissolved in 100 μL MeOH in a LC-MS vial. Calibration standards and quality control samples were prepared spanning a range of 25 ng/ml to 1250 ng/ml IKE in MeOH. Peak integration and data analysis were performed. Using the standard curve, IKE concentration in the sample was determined.

Measurement of IKE PEG-PLGA Cellular Activity

DLBCL cells or HT-1080 cells were plated at 2,000 cells per well in white 384-well plates (32 μL per well) in technical duplicates and incubated overnight. The cells were then treated with 8 μL medium containing a two-fold dilution series of vehicle 1 (DMSO), IKE, fer-1, vehicle 2 (unfunctional PEG-PLGA nanoparticles), or IKE PEG-PLGA nanoparticles. The final concentration of IKE in PEG-PLGA nanoparticles was measured by LC-MS as described in the sections below. After 24 h incubation with compounds, 40 μL of 50% CellTiter-Glo (Promega) 50% cell culture medium was added to each well and incubated at room temperature with shaking for 15 min. Luminescence was measured using a Victor X5 plate reader (PerkinElmer). All cell viability data were normalized to the DMSO vehicle condition. Experiments were performed in three independent times with different passages for each cell line. From these data, dose-response curves and IC_{50} values were computed using Prism 7.0 (GraphPad).

Kinetics of IKE Release from PEG-PLGA Nanoparticles

200 μL newly generated IKE PEG-PLGA nanoparticles were mixed with 800 μL PBS solution. They were incubated on a shaker at 37°C. Samples were collected followed by centrifugation at 10,000 x *g* for 10 min. The obtained supernatant was evaporated using a GeneVac. The obtained residues were resuspended in 100 μL methanol and analyzed with LC-MS with the methods described above. Peak integration and data analysis were performed to quantify released IKE concentration in the samples.

Solubility Measurements

Solubility measurement samples were prepared in a 96-well Corning Costar plate with two at 1% and 5% DMSO v/v with a total sample volume of 200 μL in MilliQ water. A BMG Labtech NEPHELOstar nephelometer was used to measure turbidity of the samples with the following parameters per the instrument manufacturer: Gain = 80, Laser Focus= 2.50 mm, and Laser Intensity = 90%. Samples were shaken in the nephelometer by orbital shaking for 3s prior to the turbidity measurement. Sample values were blanked in the instrument software using the corresponding water and DMSO condition values. Turbidity 4000 NTU Calibration Standard- Formazin (Millipore-Sigma) was used as a positive control for all turbidity measurements. The turbidity of each sample was measured within 20 minutes of initial preparation. After the initial measurement, the sample plates were covered with aluminum sealing film and allowed to sit overnight at room temperature prior to re-measuring.

IKE Synthesis

IKE was synthesized using methods previously reported(Larraufie et al., 2015) except that the reduction step of nitrobenzene to aniline was modified, which is described here. To a solution of substituted nitrobenzene (1 equiv.) in MeOH (0.1 M), Pd/C (0.2 equiv.) were added. The reaction mixture was gas exchanged with hydrogen, then stirred at room temperature overnight under 1 atm

hydrogen gas. Upon completion, the mixture was filtered with celite and concentrated under vacuo. The resulting mixture was purified by combiflash 0-10% methanol/dichloromethane to afford the corresponding aniline. The characterization of the final product IKE was:

^{1}H NMR (400 MHz, Dimethyl sulfoxide-*d6*) δ 8.31 (ddd, *J* = 8.0, 1.5, 0.6 Hz, 1H), 8.07 (dd, *J* = 8.7, 2.3 Hz, 1H), 8.01 (d, *J* = 2.2 Hz, 1H), 7.83 (ddd, *J* = 8.4, 7.0, 1.5 Hz, 1H), 7.80 – 7.73 (m, 1H), 7.69 (s, 1H), 7.54 (ddd, *J* = 8.2, 7.0, 1.3 Hz, 1H), 7.29 – 7.21 (m, 2H), 7.25 – 7.13 (m, 2H), 6.98 (s, 1H), 6.93 – 6.83 (m, 2H), 5.48 (d, *J* = 17.6 Hz, 1H), 5.36 (d, *J* = 17.6 Hz, 1H), 5.32 (s, 2H), 4.78 – 4.68 (m, 1H), 4.63 (s, 2H), 3.62 (s, 1H), 3.44 (d, *J* = 16.3 Hz, 4H), 3.29 (d, *J* = 14.0 Hz, 1H), 3.22 (d, *J* = 14.0 Hz, 1H), 2.50-2.13 (m, 4H), 1.28 (dd, *J* = 16.2, 6.0 Hz, 6H). MS (m/z): $[M]^+$ calculated for $C_{35}H_{35}ClN_6O_5$, 655.14; found 655.24. HPLC detected purity: 99%

Mass Spectrometry-Based Untargeted Lipidomics

Sample Preparation In Vitro Study

Lipids were extracted from each sample as described below. 5 million cells treated with DMSO, 1 μM IKE, 500 nM IKE with or without 10 μM fer-1 and 10 μM β-Me for 24 hours were homogenized in 250 μL cold methanol containing 0.1% butylated hydroxyl toluene (BHT) with micro tip sonicator. Homogenized samples were transferred to fresh glass tubes containing 850 μL of cold methyl-tert-butyl ether (MTBE) and vortex-mixed for 30 sec. To enhance extraction efficiency of lipids, the samples were incubated overnight at 4°C on the shaker. On the next day, 200 μL of cold water was added to each sample, and incubated for 20 min on ice before centrifugation at 3,000 rpm for 20 min at 4°C. The organic layer was collected followed by drying under a gentle stream of nitrogen gas on ice and stored at -80°C until LC-MS analysis. The protein pellet was used to measure protein concentration using Bio-Rad protein assay. The samples were re-constituted in a solution containing IPA/ ACN /water (4:3:1, v/v/v) containing mixture of internal standard for further MS analysis. A quality control (QC) sample was prepared by combining 40 μL of each sample to assess the reproducibility of the features through the runs.

Ultra-High Performance Liquid Chromatography Analysis

Chromatographic separation of extracted lipids was carried out at 55°C on Acquity UPLC HSS T3 column (2.1× 150 mm, 1.8 μm) over a 17-min gradient elution. Mobile phase A consisted of ACN/water (60:40, v/v) and mobile phase B was IPA/ACN/water (85:10:5, v/v/v) both containing 10 mM ammonium acetate and 0.1% acetic acid. After injection, the gradient was held at 60% mobile phase A for 1.5 min. For the next 12 min, the gradient was ramped in a linear fashion to 100% B and held at this composition for 3 min. The eluent composition returned to the initial condition in 1 min, and the column was re-equilibrated for an additional 1 min before the next injection was conducted. The flow rate was set to 400 μL/min and Injection volumes were 5 μL using the flow-through needle mode in both positive and negative ionization modes. The QC sample was injected between the samples and at the end of the run to monitor the performance and the stability of the MS platform. This QC sample was also injected at least 5 times at the beginning of the UPLC/MS run, in order to condition the column.

Mass Spectrometry Analysis

The Synapt G2 mass spectrometer (Waters, Manchester, U.K.) was operated in both positive and negative electrospray ionization (ESI) modes. For positive mode, a capillary voltage and sampling cone voltage of 3 kV and 32 V were used. The source and desolvation temperature were kept at 120°C and 500°C, respectively. Nitrogen was used as desolvation gas with a flow rate of 900 L/hr. For negative mode, a capillary voltage of -2 kV and a cone voltage of 30 V were used. The source temperature was 120°C, and desolvation gas flow was set to 900 L/hr. Dependent on the ionization mode the protonated molecular ion of leucine encephalin ($[M+H]^+$, m/z 556.2771) or the deprotonated molecular ion ($[M-H]^-$, m/z 554.2615) was used as a lock mass for mass accuracy and reproducibility. Leucine enkephalin was introduced to the lock mass at a concentration of 2 ng/μL (50% ACN containing 0.1% formic acid), and a flow rate of 10 μL/min. The data was collected in duplicates in the centroid data independent (MS^E) mode over the mass range m/z 50 to 1600 Da with an acquisition time of 0.1 seconds per scan.

The QC samples were also acquired in enhanced data independent ion mobility (IMS-MS^E) in both positive and negative modes for enhancing the structural assignment of lipid species. The ESI source settings were the same as described above. The traveling wave velocity was set to 650 m/s and wave height was 40 V. The helium gas flow in the helium cell region of the ion-mobility spectrometry (IMS) cell was set to 180 mL/min to reduce the internal energy of the ions and minimize fragmentation. Nitrogen as the drift gas was held at a flow rate of 90 mL/min in the IMS cell. The low collision energy was set to 4 eV, and high collision energy was ramping from 25 to 65 eV in the transfer region of the T-Wave device to induce fragmentation of mobility-separated precursor ions.

Data Pre-processing and Statistical Analysis

All raw data files were converted to netCDF format using DataBridge tool implemented in MassLynx software (Waters, version 4.1). Then, they were subjected to peak-picking, retention time alignment, and grouping using XCMS package (version 3.2.0) in R (version 3.5.1) environment. For the peak picking, the CentWave algorithm was used with the peak width window of 2-25 s. For peak grouping, bandwidth and m/z-width of 2 s and 0.01 Da were used, respectively. After retention time alignment and filling missing peaks, an output data frame was generated containing the list of time-aligned detected features (m/z and retention time) and the relative signal intensity (area of the chromatographic peak) in each sample. Technical variations such as noise were assessed and removed from extracted features' list based on the ratios of average relative signal intensities of the blanks to QC samples (blank/QC >1.5). Also, peaks with variations larger than 30% in QCs were eliminated. Multivariate and univariate analyses were performed using (version 4.0) and in R (version 3.5.1) environment. Group differences were calculated using VIP scores of PLS-DA model and one-way ANOVA ($p < 0.05$) and false discovery rate of 5% to control for multiple comparisons.

Structural Assignment of Identified Lipids

Identification and structural characterization of significant lipid features were confirmed with LipoStar(Goracci et al., 2017) (Version 1.0.4, Molecular Discovery, UK). Lipidomix standard (Avanti Polar Lipids, INC., Alabaster, AL, USA) and quality control samples were analyzed in LipoStar with the recommended data processing parameters(Goracci et al., 2017) except MS/MS signal filtering threshold was set to 20 for both positive and negative ionization mode. The precursor ion (MS) and fragment ion information obtained by data independent MS (MS^E) were automatically annotated using LipoStar database library with mass tolerances of 5 ppm and 10 ppm, respectively. Annotated lipid species with the highest score and high-confidence identification (matches between experimental and theoretical MS/MS spectra) were approved, and the identified lipids with low-confidence matches were further evaluated manually using MS^E data viewer (Version 1.3, Waters Corp., MA, USA). In case of co-eluting and isomeric lipid species (*e.g.*, triacylglycerols), all the available fragments in MS/MS spectra data were reported. However, if fragments for fatty acyl compositions of lipids weren't clear, the lipid species were annotated as sum of total number of carbons and double bonds (e.g. PC 32:2).

Untargeted Lipidomics Study In Vivo

25 mg frozen tissue was homogenized in 15 μL/mg pre-chilled methanol containing 0.1% butylated hydroxyl-toluene (BHT) at speed 5 for 30 secs using a Bead Ruptor 4 (OMNI International). Then, 300 μL of tissue lysate were transferred to a glass vials containing 1,000 μL ice-cold methyl-tert-butyl ether (MTBE) and vortex-mixed for 30 sec. The sample are stored in the -20°C freezer overnight to enhance lipids extraction. The following day, 250 μL of ice-cold methanol was added to each sample and vortex-mixed for 30 sec vigorously. Then, samples were incubated on dry ice for 20 min on the shaker followed by centrifuge at 3,000 rpm for 20 min at 4°C. Finally, 1,000 μL of upper phase containing lipids were transferred to fresh glass vials, and evaporated to dryness under the stream of N_2 gas. The samples were re-constituted in a solution containing IPA/ ACN /water (4:3:1, v/v/v) containing mixture of internal standard for further MS analysis. The other steps including LC-MS analysis and data processing are the same as *in vitro* lipidomic analysis as mentioned above.

MetScape analysis KEGG ID and HMDB ID.

Lpids	KEGG or HMDB ID	Full name
FA 14:0	C06424	Myristic acid
FA 16:1	C08362	Palmitoleic acid
FA 18:1	C00712	Oleic acid
FA 18:2	C01595	Linoleic acid
FA 18:3	C06426	Gamma-Linolenic acid
FA 20:1	C16526	Eicosenoic acid
FA 20:2	C16525	Eicosadienoic acid
FA 20:3	C03242	8,11,14-Eicosatrienoic acid
FA 20:4	C00219	Arachidonic acid
FA 20:5 , EPA	C06428	Eicosapentaenoic acid
FA 22:1	C08316	Erucic acid
FA 22:4	C16527	Adrenic acid
FA 22:5	C16513	Docosapentaenoic acid
FA 22:6	C06429	Docosahexaenoic acid
FA 22:0	C08281	Behenic acid
FA 24:0	C08320	Tetracosanoic acid
LPC 18:1	HMDB0002815	LysoPC(18:1(11Z))
LPE 18:1	HMDB0011506	LysoPE(18:1(9Z)/0:0)
PC 16:1/16:1	HMDB0008002	PC(16:1(9Z)/16:1(9Z))
PI 18:2/20:3	HMDB0009854	PI(18:2(9Z,12Z)/20:3(5Z,8Z,11Z))
FA 16:0	C00249	Palmitic acid
FA 17:0	HMDB0002259	Heptadecanoic acid
FA 18:0	C01530	Stearic acid
FA 24:1	C08323	Nervonic acid
DAG 34:1	HMDB0007102	DG(16:0/18:1(9Z)/0:0)
PE 16:1/18:2	HMDB0008961	PE(16:1(9Z)/18:2(9Z,12Z))
PC 16:1/18:2	HMDB0008006	PC(16:1(9Z)/18:2(9Z,12Z))
MAG 18:1	HMDB0011567	MG(18:1(9Z)/0:0/0:0)
MAG 16:0	HMDB0011533	MG(0:0/16:0/0:0)

(*Continued on next page*)

Continued

Lpids	KEGG or HMDB ID	Full name
DAG 34:2	HMDB0007103	DG(16:0/18:2(9Z,12Z)/0:0)
DAG 16:0/20:2	HMDB0007109	DG(16:0/20:2(11Z,14Z)/0:0)
DAG 18:1/18:2	HMDB0007190	DG(18:1(11Z)/18:2(9Z,12Z)/0:0)
LPE 18:1	HMDB0011506	LysoPE(18:1(9Z)/0:0)
TAG 16:0/20:4/20:5	HMDB0044553	TG(16:0/20:4(8Z,11Z,14Z,17Z)/20:5(5Z,8Z,11Z,14Z,17Z))
DAG 18:2/20:1	HMDB0007253	DG(18:2(9Z,12Z)/20:1(11Z)/0:0)
PC 16:1/16:1	HMDB0008002	PC(16:1(9Z)/16:1(9Z))
PC 16:1/18:2	HMDB0008006	PC(16:1(9Z)/18:2(9Z,12Z))
PE 16:0/16:1	HMDB0008924	PE(16:0/16:1(9Z))
PE 16:0/18:1	HMDB0008927	PE(16:0/18:1(9Z))
PS 34:3	HMDB0012409	PS(18:3(9Z,12Z,15Z)/16:0)
LPC 18:1	HMDB0002815	LysoPC(18:1(9Z))

QUANTIFICATION AND STATISTICAL ANALYSIS

T-test, one-way ANOVA, and two-way ANOVA were performed in R (version 3.5.1) environment and GraphPad Prism7 with significance and confidence level 0.05 (95% confidence interval).

MetScape analysis is performed on MetScape version 3.1.

DATA AND SOFTWARE AVAILABILITY

Please follow the Key Resources Table for software downloading. Raw mass spectrometry data files and annotated lipid feature intensities are available in Metabolights (http://www.ebi.ac.uk/metabolights/).

Cell Chemical Biology, Volume *26*

Supplemental Information

Imidazole Ketone Erastin Induces Ferroptosis and Slows Tumor Growth in a Mouse Lymphoma Model

Yan Zhang, Hui Tan, Jacob D. Daniels, Fereshteh Zandkarimi, Hengrui Liu, Lewis M. Brown, Koji Uchida, Owen A. O'Connor, and Brent R. Stockwell

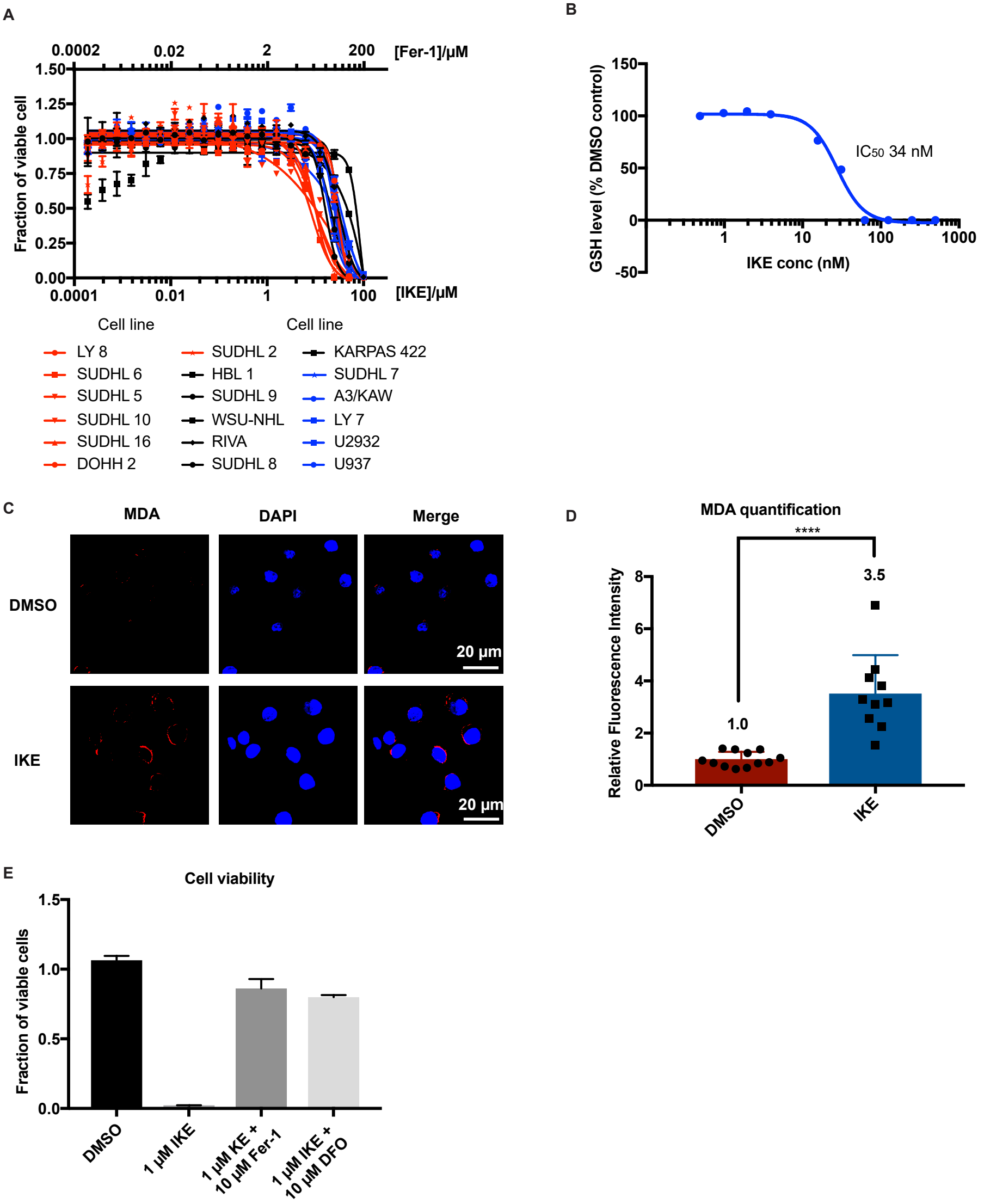

Figure S1. *in vitro* study of IKE. Related to Figure 1 and results section. (A) IKE-induced DLBCL cell death was rescued by co-treatment with Fer-1. The cell viability was measured by co-treating cells with a two-fold series dilution of IKE (starting from 100 μM) and two-fold series dilution of Fer-1 (starting from 200 μM) for 24 hours followed by a Cell Titor-Glo luminescent cell viability test. The x-axis shows the concentration of IKE and Fer-1 individually. Sensitive (red), moderately resistant (black), and resistant (blue) cell lines were classified by IKE sensitivity test shown in Figure 1 B. Data are plotted as the mean ± s.d., *n*=2 biologically replicates. Three independent experiments were performed with similar results. (B) GSH depletion curve measured by incubating SUDHL6 cells with 2-fold series dilution of IKE for 24 hours. The average IC_{50} of IKE induced GSH depletion by three biological independent experiment was 34 nM. (C) and (D) Immunofluorescence intensity of MDA in SUDHL6 cells with DMSO or 10 μM IKE treatment for 6 hours indicated 3.4-fold increased MDA upon IKE treatment. Immunofluorescence intensity was quantified on individual cells. **** P<0.0001 by t test.

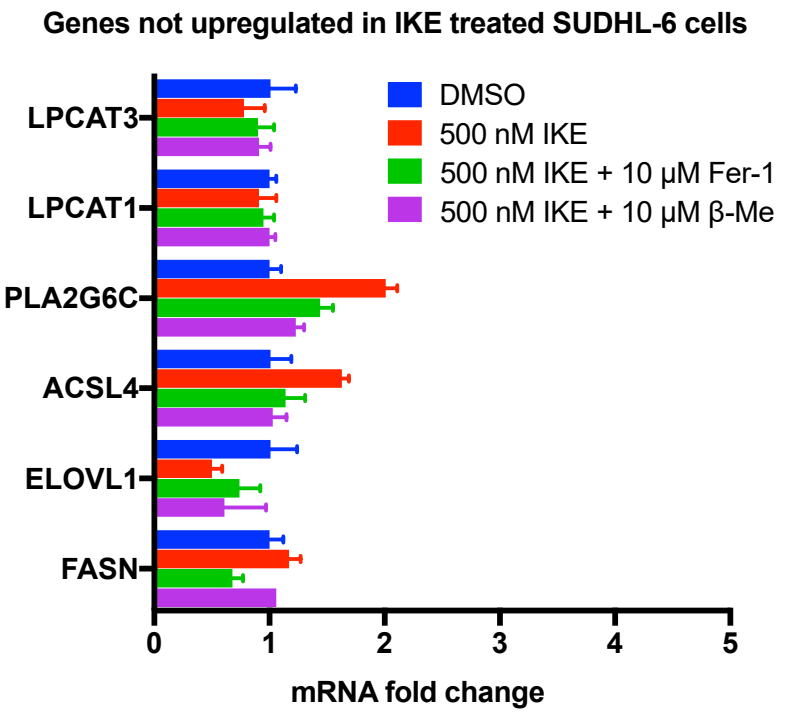

Figure S2. Fold change in expression of *FASN*, *ELOVL1*, *ACSL4*, *PLA2G6C*, *LPCAT1*, and *LPCAT3* with 500 nM IKE treatment, 500 nM IKE with 10 μM fer-1 cotreatment, and 500 nM with 10 μM β-Me cotreatment comparing with DMSO control in SUDHL-6 cells was determined by RT-qPCR. Related to Figure 2 and reuslts section.

A

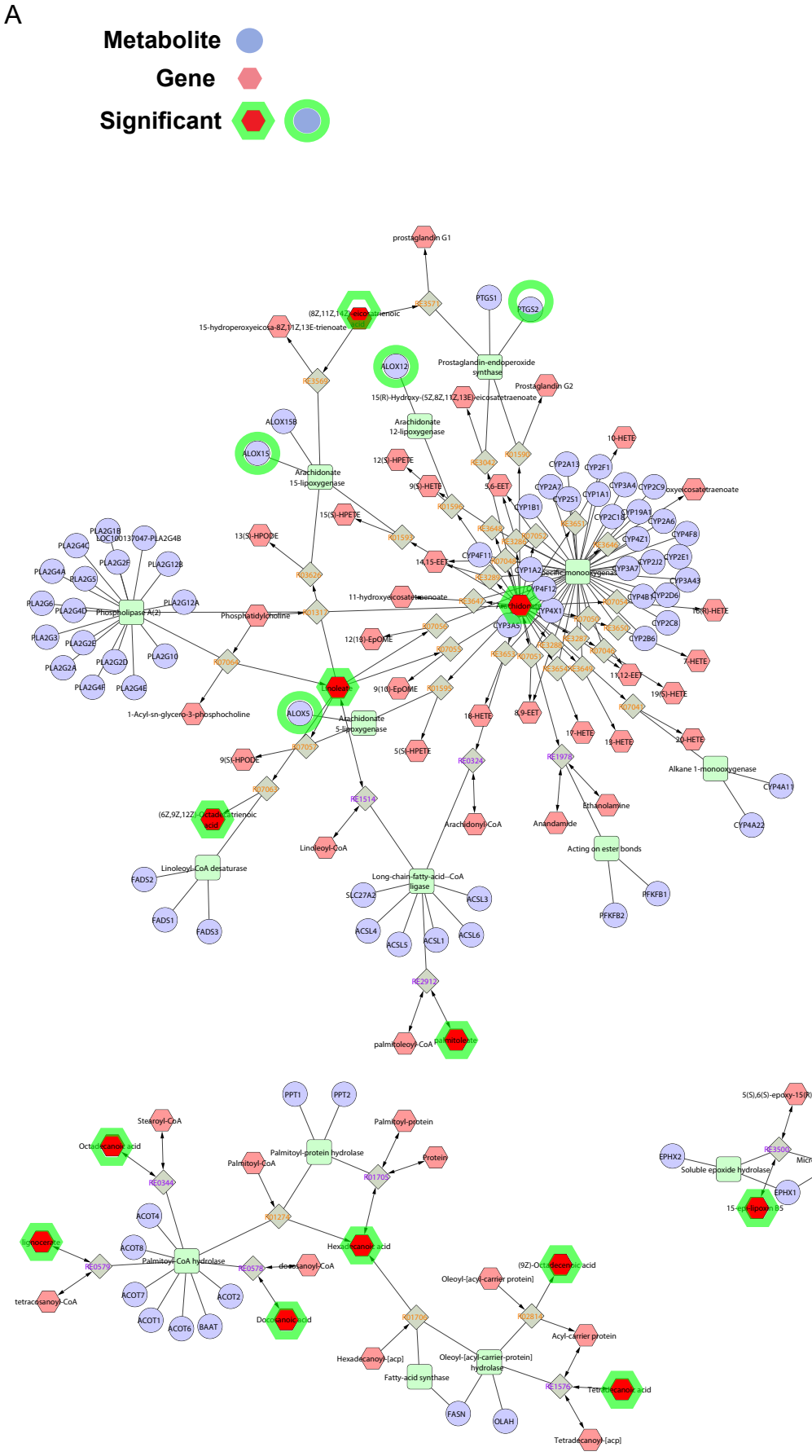

B

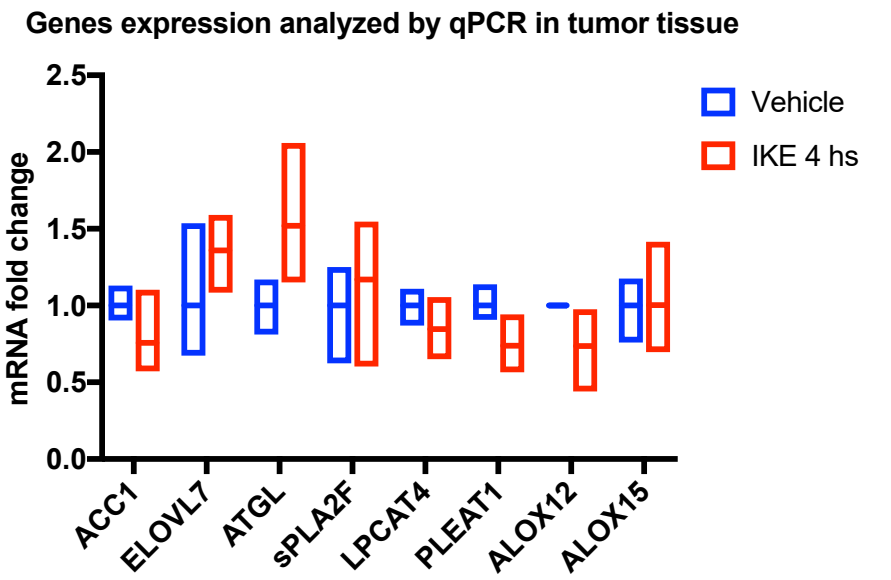

C

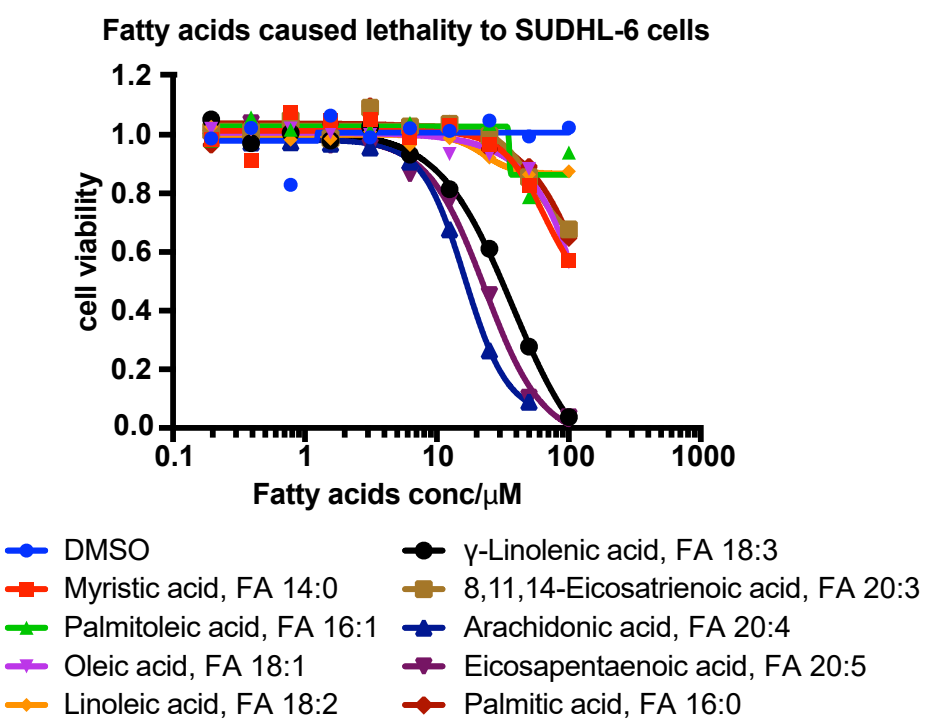

D

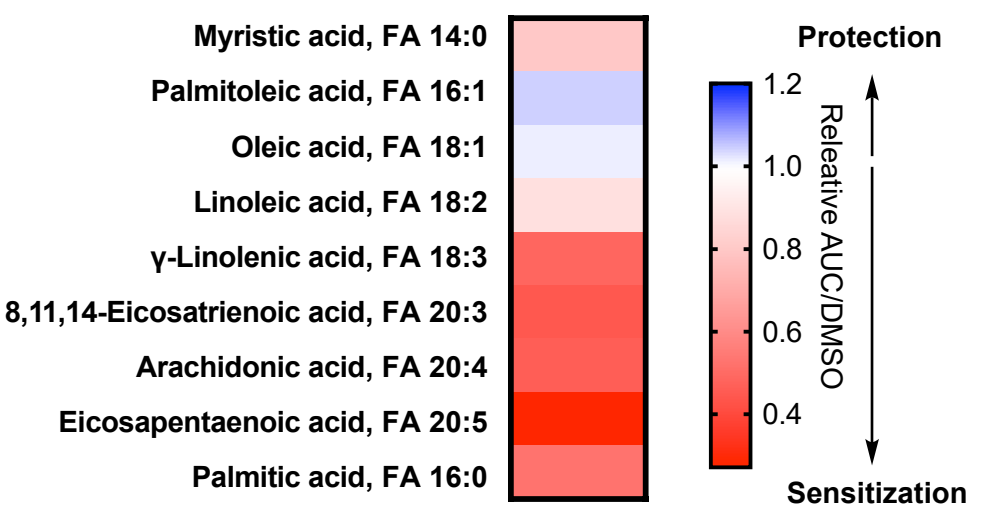

Figure S3. *in vivo* lipidomics study. Related to Figure 3 and results section. (A) Metscape network analysis of lipids identified in IKE treatment *in vivo*. Significant accumulated lipids in vivo and significant genes in ferroptosis are highlighted as green circle in the figure. (B). RT-qPCR analysis of gene expression related to lipids biosynthesis and peroxidation in tumor tissue samples from one dosage of IKE treatment comparing with vehicle treatment. (C) Dose-response curves of SUDHL-6 cells was determined by adding free fatty acids in a 10-point, two-fold dilution series for 24 hours, followed by a Cell Titor-Glo luminescent cell viability test. γ-l-linolenic acid, eicosapentaenoic acid, and arachidonic acid are toxic to cells at high concentration. (D) Dose-response curves of SUDHL-6 cells was determined by treating with IKE in a 10-point, twofold dilution series in the presence of DMSO or 10 μM free fatty acids. Relative Area Under Curve (AUC) to DMSO cotreatment was used to indicate the sensitization or protection effect of free fatty acids to IKE-induced ferroptosis.

A

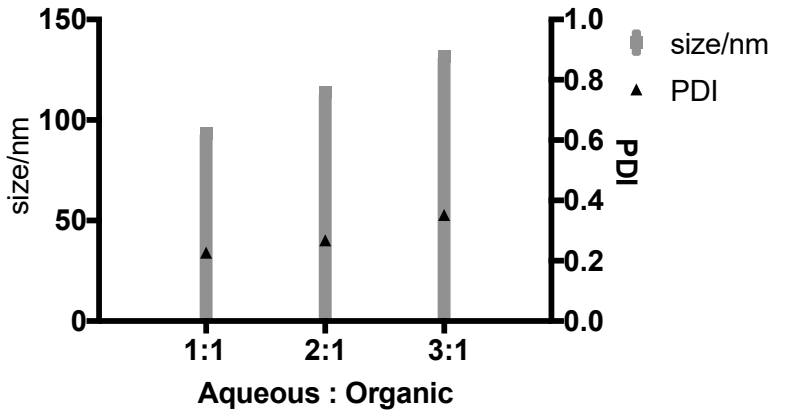

B

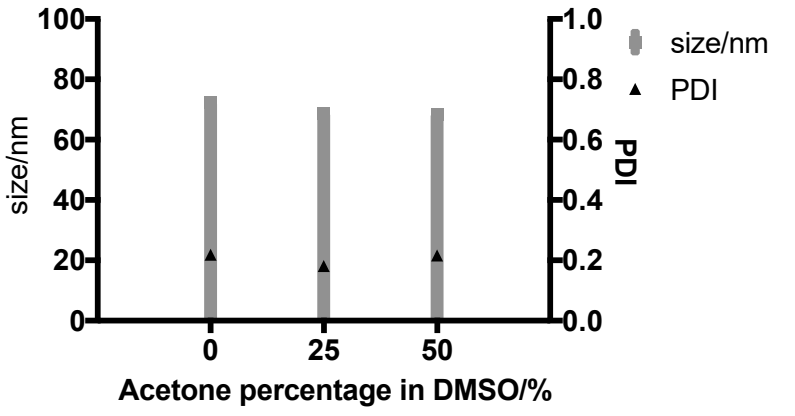

IC50 (ug/mL)	34.73	22.18	25.47

C

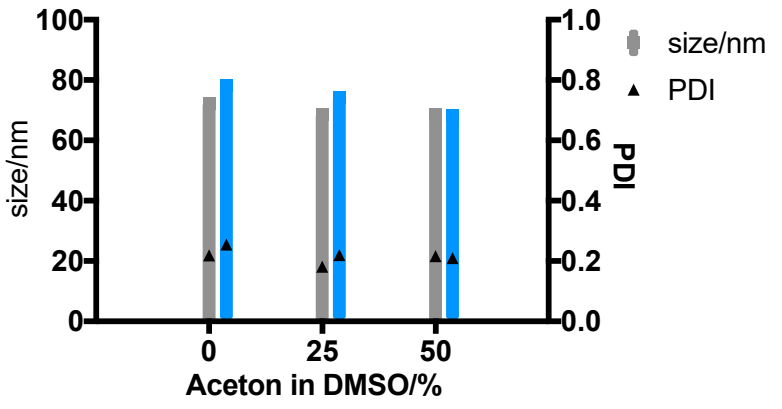

Acetone / %	0	25	50
IC50 (ug/mL)	34.73	22.18	25.47
IC50 (ug/mL)	38.93	27.78	30.72

D

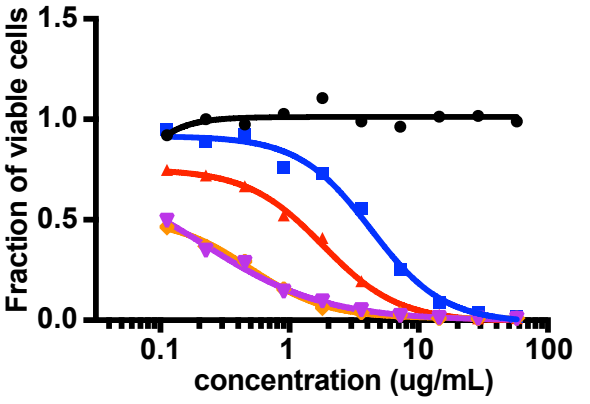

	IC50 (μg/mL)
DMSO	-
IKE PEG-PLGA (5 wt%IKE)	4.26
IKE PEG-PLGA (10 wt%IKE)	1.81
IKE PEG-PLGA (15 wt%IKE)	0.22
IKE PEG-PLGA (20 wt%IKE)	0.50

E

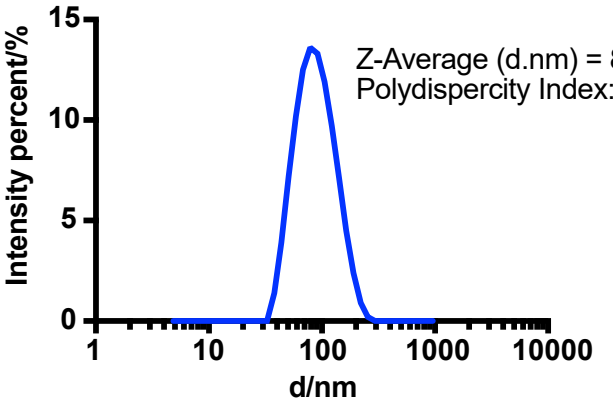

F

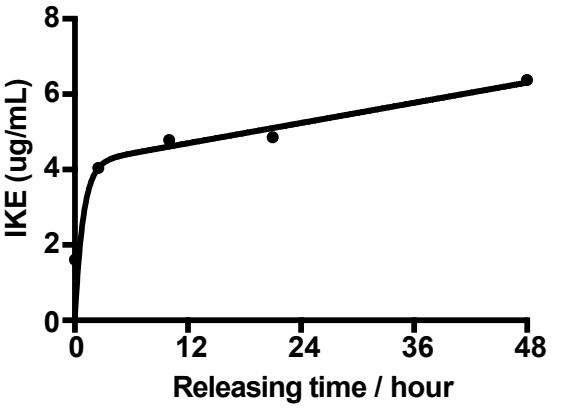

G

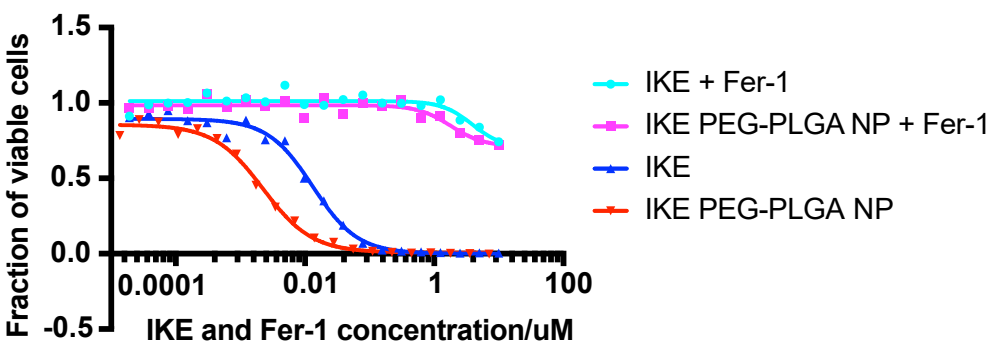

Figure S4. Optimization of PEG-PLGA NP preparation. Related to Figure 4 and results section. (A) At a flow rate of 8 mL/min and PEG-PLGA polymer concentration of 10 mg/mL in DMSO, with aqueous: organic (water: DMSO) ratio increases, the average diameter of PEG-PLGA nanoparticles formulated by NanoAssemblr increased. (B) At a flow rate of 8 mL/min, PEG-PLGA polymer concentration of 10 mg/mL, and aqueous: organic ratio of 1: 1, IKE PEG-PLGA NP prepared from 25% acetone/DMSO has relatively smaller IC50 comparing with 0% acetone/DMSO and 50% acetone/DMSO, indicating higher IKE encapsulation rate in 25% acetone/DMSO. All three solvents produced IKE PEG-PLGA NP with size smaller than 100 nm and polydispersity index (PDI) around 0.2. (C) After concentration using filter units with concentration factors up to 20, PEG-PLGA NP's average diameter and PDI weren't significantly increased. (D) Upon different initial IKE loading in PEG-PLGA NP formulation, 15 wt% IKE showed the highest potency and was used in the following experiments. E) With condition of 10 mg/mL PEG-PLGA polymer and 1.5 mg/mL IKE dissolved in 25% acetone/DMSO organic phase and mixed with water phase at flow rate of 8 mL/min followed by purification with dialysis and concentration with centrifugation, IKE PEG-PLGA NP has average diameter of 82.49 nm and PDI 0.174. (F) IKE release rate measured by LC-MS showed controlled release of IKE from PEG-PLGA NP. (G) IKE and IKE PEG-PLGA NP-induced DLBCL cell death was rescued by co-treatment with Fer-1. The cell viability was measured by co-treating cells with a two-fold series dilution of IKE (starting from 10 μM) and two-fold series dilution of Fer-1 (starting from 10 μM) for 24 hours followed by a Cell Titor-Glo luminescent cell viability test. The x-axis shows the concentration of both IKE and Fer-1. Data are plotted as the mean ± s.d., *n*=2 biologically replicates. Three independent experiments were performed with similar results.

A

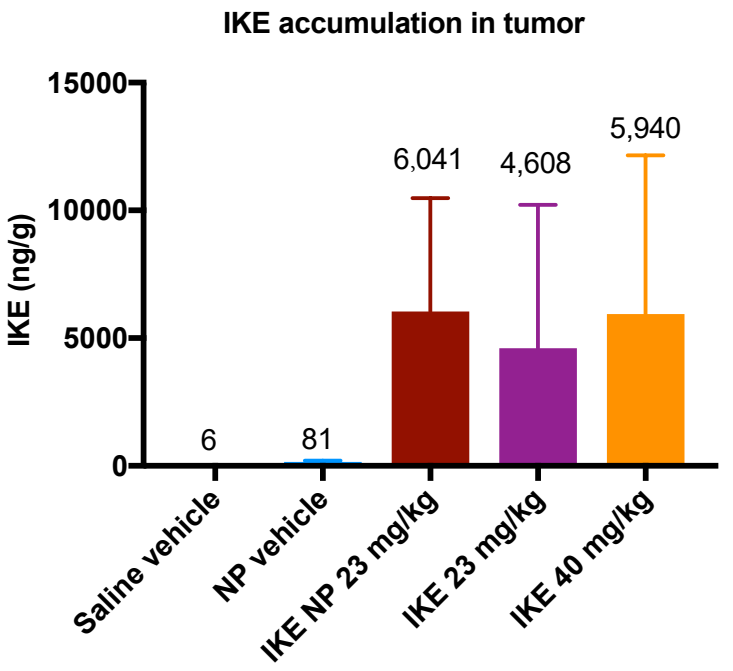

B

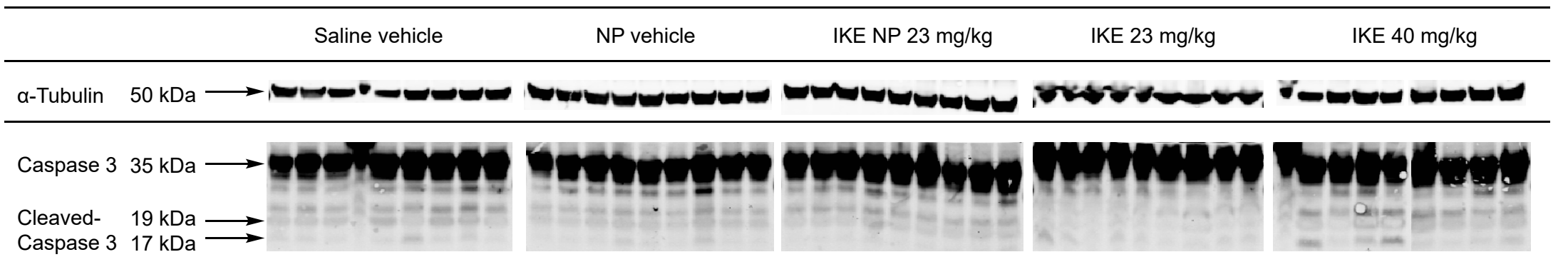

Figure S5. IKE efficacy study. Related to results section. (A) LC-MS analysis of tumor IKE concentration showed IKE NP 23 mg/kg treated mice have higher tumor IKE accumulation comparing with IKE 23 mg/kg group. Tumor samples were from mice treated with saline vehicle, NP vehicle, IKE NP 23 mg/kg, IKE 23 mg/kg, and IKE 40 mg/kg daily for 14 days and sacrificed after 3 hours of the final dosage. (B) Western blot analysis of tumor tissue from the efficacy study showed there was no cleaved-caspase 3 increase upon IKE and IKE NP treatment for 14 days. Tumor samples of 9 individual mouse from each group were analyzed in western blot.

Supplementary Table 1. IKE distribution in plasma through IP, IV, and PO administration routes. Related to STAR Methods “Pharmacokinetic analysis in mice with three different administration routes”.

	Tmax h	Cmax ng/mL	half-life h	Tlast h	Clast ng/mL	AUClast h*ng/mL
IP	0.31	19515	1.82	8	1527	53898
IV	0	11384	1.31	8	16	16983
PO	0.72	5203	0.96	8	48	5723

Supplementary Table 2. IKE distribution in plasma and tumor tissue through IP administration. Related to STAR Methods “Pharmacokinetic and pharmacodynamic analysis in NCG mice bearing SUDHL-6 xenograft” and Figure 3.

	Tmax h	Cmax ng/mL	half-life h	Tlast h	Clast ng/mL	AUClast h*ng/mL
Plasma	1.35	5185	1.83	24	30	10926
Tumor	3.30	2516	3.50	24	283	9857